

IMPACT OF *Chandra* CALIBRATION UNCERTAINTIES ON GALAXY CLUSTER TEMPERATURES:
APPLICATION TO THE HUBBLE CONSTANTERIK D. REESE^{1,2}, HAJIME KAWAHARA^{2,3}, TETSU KITAYAMA⁴, NAOMI OTA⁵, SHIN SASAKI³, AND YASUSHI SUTO^{2,6,7}

ABSTRACT

We perform a uniform, systematic X-ray spectroscopic analysis of a sample of 38 galaxy clusters with three different *Chandra* calibrations. The temperatures change systematically between calibrations. Cluster temperatures change on average by roughly $\sim 6\%$ for the smallest changes and roughly $\sim 13\%$ for the more extreme changes between calibrations. We explore the effects of the *Chandra* calibration on cluster spectral properties and the implications on Sunyaev-Zel'dovich effect (SZE) and X-ray determinations of the Hubble constant. The Hubble parameter changes by $+10\%$ and -13% between the current calibration and two previous *Chandra* calibrations, indicating that changes in the cluster temperature basically explain the entire change in H_0 . Although this work focuses on the difference in spectral properties and resultant Hubble parameters between the calibrations, it is intriguing to note that the newer calibrations favor a lower value of the Hubble constant, $H_0 \sim 60 \text{ km s}^{-1} \text{ Mpc}^{-1}$, typical of results from SZE/X-ray distances. Both galaxy clusters themselves and the details of the instruments must be known precisely to enable reliable precision cosmology with clusters, which will be feasible with combined efforts from ongoing observations and planned missions and observatories covering a wide range of wavelengths.

Subject headings: cosmic background radiation – cosmology: observations – distance scale – X-rays: galaxies: clusters

1. INTRODUCTION

Galaxy clusters have played a major role in determining cosmological parameters. Abundances of galaxy clusters have placed useful constraints on the fluctuation amplitude, σ_8 , and the matter density of the universe, Ω_M (e.g., Henry & Arnaud 1991; Viana & Liddle 1996; Bahcall et al. 1997; Eke et al. 1998; Borgani et al. 2001; Reiprich & Böhringer 2002; Schuecker et al. 2003; Henry 2004; Mantz et al. 2008; Vikhlinin et al. 2009; Mantz et al. 2010; Rozo et al. 2010). Gas fraction measurements of baryonic to total mass have also placed useful constraints on Ω_M when combined with D/H abundance measurements of Ly α clouds and big bang nucleosynthesis predictions (e.g., White et al. 1993; David et al. 1995; White & Fabian 1995; Neumann & Böhringer 1997; Squires et al. 1997; Evrard 1997; Myers et al. 1997; Ettori & Fabian 1999; Mohr et al. 1999; Grego et al. 2001; LaRoque et al. 2006). Such measurements provided one of the strongest arguments that non-relativistic matter alone does not close the universe at that time (e.g., Viana & Liddle 1996; Eke et al. 1996; Kitayama & Suto 1996, 1997). Assuming the gas fraction does not evolve enables another method of using gas fractions to place constraints on cosmological parameters (e.g., Sasaki 1996; Pen 1997; Ettori et al. 2003; Allen et al. 2004, 2008). The determination of galaxy cluster temperatures is particularly important because it is widely used to infer the gravitational mass of clusters.

In the early 1970s, Sunyaev & Zel'dovich (1970, 1972) discussed the inverse Compton scattering of cosmic microwave background (CMB) photons off of energetic electrons of the hot cluster gas causing a small ($\lesssim 1\text{mK}$) distortion in the CMB spectrum, now known as the Sunyaev-Zel'dovich effect (SZE) (for reviews see, Carlstrom et al. 2002; Birkinshaw 1999; Rephaeli 1995; Sunyaev & Zeldovich 1980). The SZE is independent of redshift making it an attractive tool to explore the high redshift universe. Analysis of both SZE and X-ray data of galaxy clusters provides a method of determining a direct distance to galaxy clusters (Cavaliere et al. 1977; Gunn 1978; Silk & White 1978; Cavaliere & Fusco-Femiano 1978; Birkinshaw 1979). These distances are independent of the extragalactic distance ladder and do not rely on standard candles or rulers. SZE/X-ray distances depend only on the properties of highly ionized plasmas. The promise of direct distances, in large part, provided incentive to measure the small SZE signal.

Recently, anisotropies of the CMB, the Hubble diagram of type Ia supernovae, and baryon acoustic oscillations in the galaxy power spectrum have proved to be precise indicators of cosmology. However, galaxy cluster surveys probe the growth of structure, one of the few methods to do so, and interpretation of survey yields has the potential to precisely constrain the equation of state of the dark energy (e.g., Bartlett & Silk 1994; Holder et al. 2000; Haiman et al. 2001; Majumdar & Mohr 2004). Current and future surveys of galaxy clusters in radio (ACT, SPT, APEX-SZ; e.g.,

Electronic address: erreese@physics.upenn.edu

¹ Department of Physics and Astronomy, University of Pennsylvania, 209 South 33rd Street, Philadelphia, PA, 19104, USA

² Department of Physics, The University of Tokyo, Tokyo 113-0033, Japan

³ Department of Physics, Tokyo Metropolitan University, Hachioji, Tokyo 192-0397, Japan

⁴ Department of Physics, Toho University, Funabashi, Chiba 274-8510, Japan

⁵ Department of Physics, Tokyo University of Science 1-3 Kagurazaka, Shinjuku, Tokyo 162-8601, Japan

⁶ Research Center for the Early Universe, Graduate School of Sciences, The University of Tokyo, Tokyo 113-0033, Japan

⁷ Department of Astrophysical Sciences, Princeton University, Princeton, NJ 08544, USA

Fowler et al. 2010; Hincks et al. 2009; Fowler et al. 2007; Carlstrom et al. 2009; Lueker et al. 2010; Reichardt et al. 2009), X-ray (eROSITA; e.g., Predehl et al. 2007, 2006), and weak-lensing (Pan-STARRS, HSC, LSST, etc.; e.g., Kaiser 2004; Miyazaki et al. 2006; Ivezic et al. 2008) promise to provide unprecedented statistical samples of galaxy clusters that will enable precision cosmology with galaxy clusters. Therefore it is important to consider possible systematics inherent to using clusters as tools of cosmology.

Traditionally SZE/X-ray estimates of the Hubble parameter tend to be low (for details see, e.g., Birkinshaw 1999; Carlstrom et al. 2002), with a few exceptions (e.g., Mason et al. 2001). However, a recent study of 38 galaxy clusters using data from *Chandra* and the OVRO/BIMA SZE imaging project find $H_0 \sim 74 \text{ km s}^{-1} \text{ Mpc}^{-1}$ (Bonamente et al. 2006), consistent with other probes, such as the *Hubble Space Telescope* (*HST*) H_0 key project (Freedman et al. 2001), supernova results (e.g., Hicken et al. 2009), and recent CMB primary anisotropy results (e.g., Komatsu et al. 2009, 2010). Previous work using the same SZE data but *ROSAT* and *ASCA* X-ray data for 18 galaxy clusters find $H_0 \sim 60 \text{ km s}^{-1} \text{ Mpc}^{-1}$ (Reese et al. 2002, hereafter R02).

We explore the effects of the *Chandra* calibration on cluster X-ray spectral properties and their subsequent effects on the inferred H_0 , through an X-ray spectral analysis of *Chandra* archival data of SZE clusters. We perform a uniform, systematic spectroscopic X-ray analysis of 38 galaxy clusters, comparing the effects of three different *Chandra* calibrations on galaxy cluster properties. The clusters are chosen from a sample used for SZE/X-ray distance measurements (Bonamente et al. 2006, hereafter B06), facilitating the exploration of how the effects of the calibration affect the inferred Hubble parameter.

B06 find much less model dependence than one might naively expect for determinations of H_0 from SZE/X-ray determined distances and therefore we focus on the simplest case, the isothermal β -model (Cavaliere & Fusco-Femiano 1976, 1978). In addition, a simple isothermal model will make it easier to isolate the effects of the different *Chandra* calibrations on individual spectral properties, such as cluster gas temperature, T_e , and the X-ray cooling function, Λ , and how these differences propagate into cosmological parameter determinations. Because $H_0 \propto T_e^2/\Lambda(T_e)$, the Hubble constant provides a good test case for tracking the effects of cluster temperature on cosmological parameters.

The rest of the paper is organized as follows. We begin with a short pedagogical discussion on modeling of the X-ray emission from galaxy clusters in Section 2 with particular attention to its potential systematic uncertainties. *Chandra* data reduction and spectroscopic analysis for the three *Chandra* calibrations are discussed in Section 3. Implications for the Hubble constant are explored in Section 4 and more general implications are discussed in Section 5. *Chandra* calibrations 3.1.0, 4.1.4, and 4.2.2 are considered and are referred to more simply as 3.1, 4.1, and 4.2. Throughout this paper, all uncertainties are at 68% confidence and we adopt a flat, Λ -dominated cosmology with $\Omega_m = 0.27$ and $\Omega_\Lambda = 0.73$ consistent with recent *Wilkinson Microwave Anisotropy Probe* (*WMAP*) results (Komatsu et al. 2010, 2009). As is the convention the Hubble constant is sometimes expressed as h , defined as $H_0 = 100 h \text{ km s}^{-1} \text{ Mpc}^{-1}$.

2. MODELING X-RAY SURFACE BRIGHTNESS OF GALAXY CLUSTERS FOR ESTIMATING THE HUBBLE CONSTANT

2.1. Theoretical modeling

We start with a pedagogical discussion of X-ray emission from galaxy clusters in order to elucidate important details relevant to this work and differences within the literature. We denote the X-ray emissivity [$\text{erg s}^{-1} \text{ cm}^{-3} \text{ keV}^{-1}$] at the source as

$$\frac{d^2 L_X}{dE_{\text{source}} dV_{\text{source}}} \equiv \lambda(E_{\text{source}}, T_{\text{source}}, Z_{\text{source}}) n_e^2, \quad (1)$$

where L_X is X-ray luminosity, E is photon energy, V is volume, $T = T_e$ is the cluster temperature, Z is metallicity relative to solar, n_e is the electron density, and we use the index ‘‘source’’ for clarity to indicate variables defined at the source position (with redshift z). The function $\lambda(E_{\text{source}}; T_{\text{source}}, Z_{\text{source}})$ [$\text{erg s}^{-1} \text{ cm}^3 \text{ keV}^{-1}$] depends on the temperature T_{source} and the metal abundance Z_{source} of the source, and is given by the theoretical model.

Consider X-ray photons isotropically emitted from the source of physical size $\Delta x \Delta y \Delta \ell$ (with ℓ chosen to be along the line of sight of the observer at $z = 0$) with energy range $E_{\text{source}} \sim E_{\text{source}} + \Delta E_{\text{source}}$ for a time interval Δt_{source} . Then the total number of the photons is given by

$$\mathcal{N}_X^{\text{source}} = \frac{1}{E_{\text{source}}} \frac{d^2 L_X}{dE_{\text{source}} dV_{\text{source}}} \times \Delta E_{\text{source}} \Delta t_{\text{source}} \Delta x \Delta y \Delta \ell. \quad (2)$$

The ideal observer (with perfect efficiency) receives the same number of photons from the solid angle of the source $\Delta \Omega_{\text{obs}} \equiv \Delta \theta_x \Delta \theta_y = \Delta x \Delta y / d_A^2$ for a time interval Δt_{obs} with energy range $E_{\text{obs}} \sim E_{\text{obs}} + \Delta E_{\text{obs}}$, where those variables with index ‘‘obs’’ are defined at the observer’s frame, and d_A is the angular diameter distance to the source. If we denote the ‘‘differential’’ surface brightness of the source as

$$\frac{dS_X^{\text{theory}}}{dE_{\text{obs}}} \quad [\text{erg s}^{-1} \text{ cm}^{-2} \text{ arcmin}^{-2} \text{ keV}^{-1}], \quad (3)$$

then the number of photons in the observer’s frame is given by

$$\mathcal{N}_X^{\text{obs}} = 4\pi d_{\text{com}}^2 \frac{1}{E_{\text{obs}}} \frac{dS_X^{\text{theory}}}{dE_{\text{obs}}} \times \Delta E_{\text{obs}} \Delta t_{\text{obs}} \Delta \Omega_{\text{obs}}, \quad (4)$$

where d_{com} is the comoving distance to the source at redshift z . Since the number of photons in both frames is invariant, $\mathcal{N}_X^{\text{obs}} = \mathcal{N}_X^{\text{source}}$, Equations (2) and (4) are equal and we obtain

$$\begin{aligned} \frac{dS_X^{\text{theory}}}{dE_{\text{obs}}} &= \frac{1}{4\pi d_{\text{com}}^2} \frac{E_{\text{obs}}}{E_{\text{source}}} \frac{d^2 L_X}{dE_{\text{source}} dV_{\text{source}}} \frac{\Delta t_{\text{source}}}{\Delta t_{\text{obs}}} \frac{\Delta E_{\text{source}}}{\Delta E_{\text{obs}}} \frac{\Delta x \Delta y}{\Delta \Omega_{\text{obs}}} \Delta \ell \\ &= \frac{1}{4\pi d_{\text{com}}^2} \frac{1}{1+z} \frac{d^2 L_X}{dE_{\text{source}} dV_{\text{source}}} \frac{1}{1+z} (1+z) d_A^2 \Delta \ell \\ &= \frac{1}{4\pi(1+z)} \left(\frac{d_A}{d_{\text{com}}} \right)^2 \frac{d^2 L_X}{dE_{\text{source}} dV_{\text{source}}} \Delta \ell \\ &= \frac{1}{4\pi(1+z)^3} \frac{d^2 L_X}{dE_{\text{source}} dV_{\text{source}}} \Delta \ell, \end{aligned} \quad (5)$$

where we use $E_{\text{source}} = (1+z)E_{\text{obs}}$, $\Delta t_{\text{source}} = \Delta t_{\text{obs}}/(1+z)$, and $d_A = d_{\text{com}}/(1+z)$.

If the profile along the line of sight is properly taken into account, $\Delta \ell$ in the above equation will be replaced by the integration along the line of sight:

$$\begin{aligned} \frac{dS_X^{\text{theory}}}{dE_{\text{obs}}} &= \frac{1}{4\pi(1+z)^3} \int d\ell \frac{d^2 L_X}{dE_{\text{source}} dV_{\text{source}}} \\ &= \frac{1}{4\pi(1+z)^3} \int d\ell \lambda(E_{\text{source}}, T_{\text{source}}, Z_{\text{source}}) n_e^2. \end{aligned} \quad (6)$$

Then the surface brightness of the source, S_X^{theory} [erg s⁻¹ cm⁻² arcmin⁻²], defined at the observer's frame is given by

$$\begin{aligned} S_X^{\text{theory}} &= \int dE_{\text{obs}} \frac{dS_X^{\text{theory}}}{dE_{\text{obs}}} = \frac{1}{4\pi(1+z)^3} \int dE_{\text{obs}} \int d\ell \frac{d^2 L_X}{dE_{\text{source}} dV_{\text{source}}} \\ &= \frac{1}{4\pi(1+z)^4} \int d\ell \int dE_{\text{source}} \lambda(E_{\text{source}}, T_{\text{source}}, Z_{\text{source}}) n_e^2 \\ &= \frac{1}{4\pi(1+z)^4} \int d\ell \Lambda^{\text{theory}}(T_{\text{source}}) n_e^2, \end{aligned} \quad (7)$$

where the cooling function $\Lambda^{\text{theory}}(T_{\text{source}})$ [erg s⁻¹ cm³] is given by

$$\Lambda^{\text{theory}}(T_{\text{source}}) \equiv \int dE_{\text{source}} \lambda(E_{\text{source}}, T_{\text{source}}, Z_{\text{source}}). \quad (8)$$

Note that $\Lambda^{\text{theory}}(T_{\text{source}})$ indeed depends on Z_{source} as well, but we do not write it explicitly for simplicity of notation.

2.2. From observed photon counts to surface brightness

In real observations, we have to take account of the overall response function of the detector and the telescope, whose effect is expressed by the energy-dependent effective area $A(E_{\text{obs}})$ [cm²]. Then the observed number of photons per unit time per unit solid angle counted on the detector, $d^2 \mathcal{N}_X^{\text{obs}} / (dt_{\text{obs}} d\Omega_{\text{obs}})$ [counts s⁻¹ arcmin⁻²], is modeled as

$$\begin{aligned} \frac{d^2 \mathcal{N}_X^{\text{obs}}}{dt_{\text{obs}} d\Omega_{\text{obs}}} &= \int dE_{\text{obs}} \frac{1}{E_{\text{obs}}} \frac{dS_X^{\text{theory}}}{dE_{\text{obs}}} A(E_{\text{obs}}) \\ &= \int dE_{\text{source}} \frac{1}{E_{\text{source}}} \frac{dS_X^{\text{theory}}}{dE_{\text{obs}}} A(E_{\text{obs}}) \\ &= \frac{1}{4\pi(1+z)^3} \int n_e^2 d\ell \\ &\quad \times \int dE_{\text{source}} \frac{\lambda(E_{\text{source}}, T_{\text{source}}, Z_{\text{source}})}{E_{\text{source}}} A\left(\frac{E_{\text{source}}}{1+z}\right). \end{aligned} \quad (9)$$

Spectral analysis of the observed X-ray photons yields T_{source} and Z_{source} that best-fit the data.

Let us define the *effective* cooling function as

$$\begin{aligned} \Lambda^{\text{eff}}(T_{\text{source}}) &\equiv \frac{1}{A(E_{\text{obs}} = E_{\text{fid}})} \\ &\times \int_{E_{1,\text{obs}}(1+z)}^{E_{2,\text{obs}}(1+z)} dE_{\text{source}} \frac{\lambda(E_{\text{source}}, T_{\text{source}}, Z_{\text{source}})}{E_{\text{source}}} A\left(\frac{E_{\text{source}}}{1+z}\right), \end{aligned} \quad (10)$$

where E_{fid} is some fiducial energy, $E_{\text{fid}} = 1$ keV for the *Chandra* analyses presented and compared in this work, and $E_{1,\text{obs}}$ and $E_{2,\text{obs}}$ correspond to the observed energy band of the detector (or of the analysis).

Before proceeding further, a few comments should be added here. First, this quantity has units of $[\text{erg s}^{-1} \text{cm}^3 \text{keV}^{-1}] = [\text{counts s}^{-1} \text{cm}^3]$, different from that of $\Lambda^{\text{theory}} [\text{erg s}^{-1} \text{cm}^3]$. In addition to covering different energy ranges, *ROSAT* and *Chandra* treat exposure maps differently, which leads to different treatments of the ‘‘cooling function’’. Therefore one must be careful when comparing emissivity and surface brightness results even in cgs units. Of course, a ‘‘count’’ in different observatories corresponds to different energy photons, on average, so ‘‘detector’’ unit results most often can not be compared directly either. Choosing $E_{\text{fid}} = 1 \text{ keV}$ in B06 is effectively arbitrary but does roughly correspond to where *Chandra* is most sensitive and corresponds to the energy at which the exposure maps used in their analysis were computed. We follow suit and adopt $E_{\text{fid}} = 1 \text{ keV}$ for a more straight-forward comparison.

Finally the *effective* cooling function depends on Z_{source} and z in addition to T_{source} , but we write it as $\Lambda^{\text{eff}}(T_{\text{source}})$ for simplicity. Equations (9) and (10) are now combined to give

$$\frac{d^2 \mathcal{N}_X^{\text{obs}}}{dt_{\text{obs}} d\Omega_{\text{obs}}} \frac{1}{A(E_{\text{obs}} = E_{\text{fid}})} = \frac{1}{4\pi(1+z)^3} \int n_e^2 dl \times \Lambda^{\text{eff}}(T_{\text{source}}). \quad (11)$$

Comparing this equation with Equation (7), we find that if we define the quantity:

$$\mathcal{S}_X^{\text{obs}} \equiv \frac{d^2 \mathcal{N}_X^{\text{obs}}}{dt_{\text{obs}} d\Omega_{\text{obs}}} \frac{1}{A(E_{\text{obs}} = E_{\text{fid}})}, \quad (12)$$

then we obtain

$$\mathcal{S}_X^{\text{obs}} = \frac{1}{4\pi(1+z)^3} \int n_e^2 dl \times \Lambda^{\text{eff}}(T_{\text{source}}). \quad (13)$$

Again it should be noted that $\mathcal{S}_X^{\text{obs}} [\text{erg s}^{-1} \text{cm}^{-2} \text{arcmin}^{-2} \text{keV}^{-1}] (= [\text{counts s}^{-1} \text{cm}^{-2} \text{arcmin}^{-2}])$ is not directly related to the surface brightness S_X^{theory} , but this notation follows that used in the literature.⁸

In any case, if the effective cooling function is independent of the line-of-sight integral of Equation (13), such as in the isothermal case considered here, we can estimate the density squared integrated along the line of sight as

$$\frac{1}{4\pi(1+z)^4} \int n_e^2 dl = \frac{\mathcal{S}_X^{\text{obs}} [\text{counts s}^{-1} \text{cm}^{-2} \text{arcmin}^{-2}]}{(1+z)\Lambda^{\text{eff}}(T_{\text{source}}) [\text{counts s}^{-1} \text{cm}^3]}. \quad (14)$$

Even though $\mathcal{S}_X^{\text{obs}}$ and $\Lambda^{\text{eff}}(T_{\text{source}})$ are not the direct observational counterparts of S_X^{theory} and $\Lambda^{\text{theory}}(T_{\text{source}})$, respectively, their ratio may be used to estimate the left-hand-side in the above equation.

2.3. Breakdown of factors important for determining H_0 with different calibrations

As discussed previously, the X-ray emission is

$$\mathcal{S}_X^{\text{obs}} \propto \int n_e^2 \Lambda^{\text{eff}} dl \propto n_e^2 \Lambda^{\text{eff}} \Delta\ell. \quad (15)$$

Since the observed SZE temperature decrement is proportional to the pressure integrated along the line-of-sight,

$$\Delta T_{\text{SZE}} \propto f_{(\nu, T_{\text{source}})} \int n_e T_{\text{source}} dl \sim f_{(\nu, T_{\text{source}})} n_e T_{\text{source}} \Delta\ell, \quad (16)$$

the angular diameter distance, d_A , can be estimated by taking advantage of the different dependencies on n_e . The frequency dependence of the SZE, $f_{(\nu, T_e)}$, also depends on temperature when relativistic effects are considered (e.g., Itoh et al. 1998; Challinor & Lasenby 1998). Eliminating n_e in favor of $\Delta\ell$ yields

$$d_A \propto \Delta\ell \propto \left(\frac{\Delta T_{\text{SZE}}}{T_{\text{source}} f_{(\nu, T_{\text{source}})}} \right)^2 \frac{\Lambda^{\text{eff}}}{\mathcal{S}_X^{\text{obs}}}. \quad (17)$$

Therefore the estimated Hubble constant should be proportional to

$$H_{0, \text{est}} \propto \Delta\ell^{-1} \propto \frac{T_{\text{source}}^2 \mathcal{S}_X^{\text{obs}} f_{(\nu, T_{\text{source}})}^2}{\Lambda^{\text{eff}}(T_{\text{source}})} \propto \frac{T_{\text{source}}^2 f_{(\nu, T_{\text{source}})}^2}{\Lambda^{\text{eff}}(T_{\text{source}}) A(E_{\text{obs}} = E_{\text{fid}})}, \quad (18)$$

where we assume that the values of ΔT_{SZE} and $\mathcal{N}_X^{\text{obs}}$ are not affected by the change of the calibration. Details on the calculation of distances from the analysis of X-ray and SZE data can be found elsewhere (e.g., Birkinshaw et al. 1991; Birkinshaw 1999; Reese et al. 2002). The dependence of $f_{(\nu, T_{\text{source}})}$ on T_e is weak and we neglect it in the rest of this section, although we do include it in the distance and Hubble constant calculations from the data (Section 4).

⁸ In R02, some effort was made to distinguish between the observed, denoted as ‘‘detector’’, and theoretical, denoted as ‘‘cgs’’, quantities and both were presented while the B06 analysis presents only observed (detector) values.

Thus the ratio of the estimates of H_0 from two different calibrations, 1 and 2, is finally written as

$$\begin{aligned} \frac{H_{0,2}}{H_{0,1}} &= \frac{T_2^2}{\Lambda_2^{\text{eff}}(T_2) A_2(E_{\text{fid}})} \frac{\Lambda_1^{\text{eff}}(T_1) A_1(E_{\text{fid}})}{T_1^2} \\ &= \left(\frac{T_2}{T_1}\right)^2 \frac{\Lambda_1^{\text{eff}}(T_1) A_1(E_{\text{fid}})}{\Lambda_2^{\text{eff}}(T_2) A_2(E_{\text{fid}})}. \end{aligned} \quad (19)$$

Equation (19) can be rewritten in a form useful in understanding the error budget of the estimate of H_0

$$\frac{H_{0,2}}{H_{0,1}} = \left(\frac{T_2}{T_1}\right)^2 \frac{\Lambda_2^{\text{eff}}(T_1) \Lambda_1^{\text{eff}}(T_1) A_1(E_{\text{fid}})}{\Lambda_2^{\text{eff}}(T_2) \Lambda_2^{\text{eff}}(T_1) A_2(E_{\text{fid}})}, \quad (20)$$

where $\Lambda_2^{\text{eff}}(T_1)$ is the effective cooling function using the temperature from observation 1 but the effective area corresponding to observation 2. Because it enters the H_0 calculation squared, the effects of the calibration on T_e will have the greatest impact. For instance, a $\sim 10\%$ change in T_e would result in a $\sim 20\%$ change in the derived Hubble parameter.

The product of the third and fourth factors indicates the effect of the different effective areas evaluated at the same temperature (and same abundance). More specifically it is given by

$$\begin{aligned} &\frac{\Lambda_1^{\text{eff}}(T_1) A_1(E_{\text{fid}})}{\Lambda_2^{\text{eff}}(T_1) A_2(E_{\text{fid}})} \\ &= \frac{\int_{E_{1,\text{obs}}(1+z)}^{E_{2,\text{obs}}(1+z)} dE_{\text{source}} \frac{\lambda(E_{\text{source}}, T_1, Z_1)}{E_{\text{source}}} A_1\left(\frac{E_{\text{source}}}{1+z}\right)}{\int_{E_{1,\text{obs}}(1+z)}^{E_{2,\text{obs}}(1+z)} dE_{\text{source}} \frac{\lambda(E_{\text{source}}, T_1, Z_1)}{E_{\text{source}}} A_2\left(\frac{E_{\text{source}}}{1+z}\right)}. \end{aligned} \quad (21)$$

The above factors may change the inferred Hubble parameter by several percent (see Figure 1 in Section 3.2).

3. SPECTROSCOPIC TEMPERATURE OF SIZE CLUSTERS WITH *Chandra*

We determine the spectroscopic temperature of all 38 clusters used in the B06 analysis with three different versions of the calibration database and corresponding ciao versions: calibration versions 3.1.0, 4.1.4, and 4.2.2 with ciao versions 3.4, 4.1.2, and 4.2. These calibrations will be referred to as 3.1, 4.1, and 4.2 hereafter.

The most significant change between the 3.1 and 4.1 calibrations is the updated high-resolution mirror assembly (HRMA) effective area in version 4.1. A new effective area model was developed after revisiting the ground calibration data and ray-trace model, prompted, in large part, by differences in inferred temperatures of massive galaxy clusters between *Chandra* and *XMM-Newton*. The newer effective area at low energy ($E < 5$ keV) is $\lesssim 10\%$ lower than that of the older calibration.¹ The main change in calibration version 4.2 is the AXAF CCD imaging spectrometer (ACIS) contamination model.² Based on external calibration source (ECS) measurements, separate ACIS-I and ACIS-S models were developed. An offset was added to normal exponential evolution of the contamination model for ACIS-S,³ while there is no such offset applied for ACIS-I. We note that there are a lot of other minor changes between 4.1 and earlier versions, and between 4.1 and 4.2. These more minor changes also have the potential to affect changes in the estimated cluster temperatures but to a much lesser extent than the changes outlined above.

3.1. Data Reduction

All available archival *Chandra* data for the 38 galaxy clusters in our sample are used in the analysis. This includes all data used in B06 as well as observations available at the time but not included and new observations since that time that are in the public archive. There are 87 observations among the 38 galaxy clusters, not including two observations of A0267 that have $\lesssim 1$ ks of observation time that were not used. The data are summarized in Table 3. Cluster position, redshift, H I column density (Dickey & Lockman 1990), observation identification number, ACIS configuration (ACIS-I or ACIS-S), and livetime (effective integration time) are shown. Redshift references may be found in B06.

The data are reduced with each of the three different versions of the calibration database 3.4, 4.1, and 4.2. The data are processed starting with the level 1 events data, removing the cosmic ray afterglow correction, and generating a new bad pixel file that accounts for hot pixels and cosmic ray afterglows. Using the newly generated bad pixel file, the charge transfer inefficiency correction, time-dependent gain adjustment, and other standard corrections are applied to the data. The data are filtered for *ASCA* grades 0, 2, 3, 4, 6 and status=0 events and the good time interval data provided with the observations are applied. Periods of high background count rate are excised using an iterative procedure involving creating light curves in background regions with 259 s bins (following the ACIS ‘‘Blank-Sky’’

¹ http://cxc.harvard.edu/ciao/releasenotes/ciao_4.1_release.html

² http://cxc.harvard.edu/ciao/releasenotes/ciao_4.2_release.html

³ http://cxc.harvard.edu/cal/memos/contam_memo.pdf

Background File reduction), and excising time intervals that are in excess of 3σ (=rms) from the mean background count rate. This sigma clipping procedure is iterated until all remaining data lie within 3σ of the mean. The final events list is limited to energies 0.7-7.0 keV to exclude the low- and high-energy data that are more strongly affected by calibration uncertainties.

Lightcurve filtering is performed on background regions chosen for each observation. Three circular regions, masking out any intervening point sources, are used as the background regions. Investigation of deep blank-sky exposures shows that front-illuminated (FI) and back-illuminated (BI) chips have different responses (Bonamente et al. 2004). In particular, the BI chips are basically constant over the chip but there is a gradient in the FI chips that depends on the distance from the readout nodes. For observations taken in the ACIS-S configuration, the cluster observation falls on a BI chip. In these cases, background regions are chosen at the periphery of the BI chip, away from the cluster emission. For observations taken in the ACIS-I configuration, there are four main FI chips. The cluster falls on one of those chips (I3). Background regions are chosen from the three remaining chips (I0, I1, and I2), one region for each chip, using locations at the same distance from the readout nodes as the cluster.

To facilitate point source detection, images and exposure maps are constructed. Images are created by binning the data by a factor of 4, resulting in a pixel size of $1''.97$. Exposure maps are constructed for each observation at an energy of 1 keV. For clusters with multiple data sets, the observation with the longest exposure time is used for point source detection. A wavelet based source detector is used to find and generate a list of potential point sources. The list is examined by eye, removing bogus or suspect detections, and then used as the basis for our point source mask.

Spectra are extracted from the cluster using a region that encompasses 95% of the galaxy cluster counts, accounting for point sources that fall within the region of interest. The same wavelet based source detection algorithm as for point source detection is used to find the cluster by having it search for large scales (compared to the point-spread function (PSF)) and determine the initial extraction region. The center of the ellipse returned by the source detector is adopted as the center of the extraction region and the semimajor and semiminor axes of the ellipse are combined in quadrature and its square root used as the radius for the circular extraction region. Background subtracted counts are then computed in annuli out to the initial extraction radius and the region encompassing 95% of the cluster counts is adopted as the final extraction radius. This provides a formulaic method of constructing spectral extraction regions.

Calibration version 4.1 is used to construct background and spectral extraction regions that are then used for the other two reductions. This provides a uniform reduction and systematic analysis procedure that isolated the effects of the calibration. Using these regions, spectra are extracted and responses computed for each observation. Multiple observations for a given cluster each have spectra and response files that are then simultaneously fit to a thermal spectrum.

3.2. Spectral Analysis

Following Bonamente et al. (2006, 2004), XSPEC (Arnaud 1996; Dorman & Arnaud 2001) is used to model the intracluster medium (ICM) with a Raymond–Smith spectrum (Raymond & Smith 1977) accounting for galactic extinction, with solar abundances of Feldman (1992), and cross sections of Balucinska-Church & McCammon (1992) with an updated He cross section (Yan et al. 1998). The analysis uses data in the 0.7-7.0 keV energy range. We use the “cstat” statistic in XSPEC, essentially the so-called Cash-statistic (Cash 1979), to properly account for low count spectral bins. Using the χ^2 statistic in such cases will result in biased spectral parameters. We perform a Markov Chain Monte Carlo (MCMC) analysis, allowing us to compute proper uncertainties on the X-ray cooling function, Λ_{eff} , which also enters the distance calculation and is derived from the spectral parameters from the MCMC chain.

A simultaneous fit is performed to all data sets of a given cluster. Responses for each individual cluster observation may be quite different even for the same cluster. In particular, the FI and BI ACIS chips show considerably different responses. Therefore, for clusters with multiple observations, each individual observation is modeled independently, using their individual response and background spectra. Normalizations of the model are allowed to vary for each data set while the temperature and abundance are linked between the different data sets. Redshift and column density are held fixed, adopting the Dickey & Lockman (1990) N_{H} values (See Table 3).

Markov chains are run for 100,000 iterations. We drop the initial 5000 iterations for the burn-in period but the results are insensitive to that choice. The X-ray cooling function, Λ_{eff} , is computed at each step in the Markov chain, enabling the folding of uncertainties of the spectral parameters to the computed Λ_{eff} . Best-fit parameters and confidence intervals are computed from the cumulative distribution with 50%, 16%, and 84% probability, corresponding to the median and 68% confidence interval. The resultant probability distribution functions for each fit and derived parameter of each cluster are visually inspected. Convergence and mixing are checked with the Geweke Z -statistic (Geweke 1992).

For clusters with multiple observations, a weighted average effective area as a function of energy is used to compute the X-ray cooling function. The weighted average effective area, $A_{\text{avg}}(E)$, is the average effective area weighted by the livetime (effective integration time) of each observation, $A_{\text{avg}}(E) = (\sum A_i(E) * t_i) / \sum t_i$, where $A_i(E)$ is the effective area of observation i , t_i is the livetime of observation i , and the sum is over the number of observations for that cluster. The weighted average effective area is used to compute Λ_{eff} at each step in the Markov chain and determine the best-fit value and 68% confidence interval.

3.3. Spectral Results

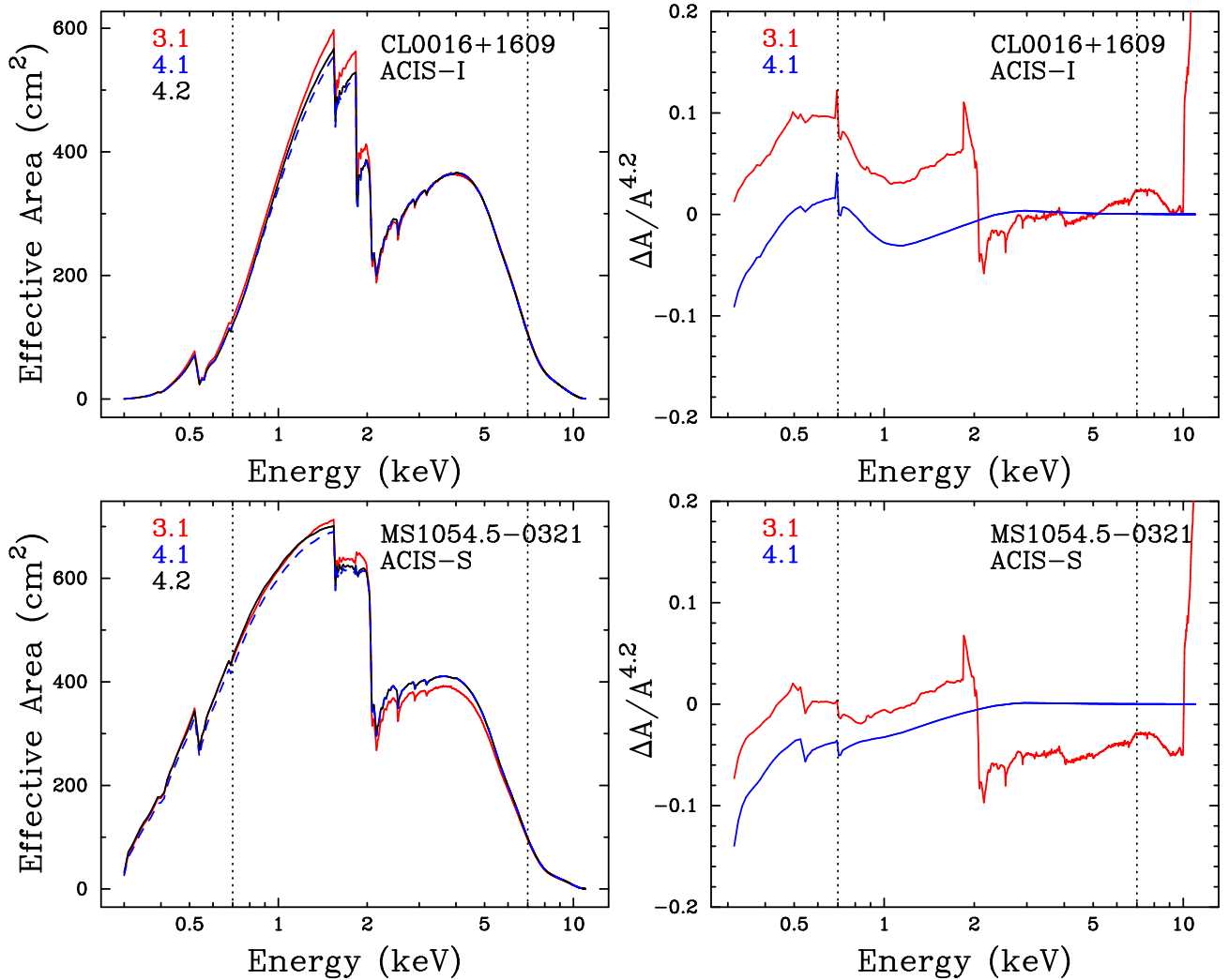


FIG. 1.— Comparison of the effective areas for the 3.1 (red), 4.1 (blue), and 4.2 (black) calibrations for examples of ACIS-I (CL0016+16; top) and ACIS-S (MS1054.5-0321; bottom) observations. The fractional residuals from the 4.2 effective area are shown in the right hand panels, $\Delta A/A^{4.2} = (A^x - A^{4.2})/A^{4.2}$, where x is either 3.1 (red) or 4.1 (blue). In addition to the changes seen between 1 and 2 keV in both ACIS-I and ACIS-S observations, ACIS-S observations also exhibit appreciable differences between the 3.1 and 4.1/4.2 calibrations in the 2–5 keV range. The vertical dotted lines mark the 0.7-7.0 keV energy range used in this analysis.

The newest calibration version, 4.2, will be used as the baseline for comparison with the other two calibrations throughout the analysis. We define the mean ratio of parameter P between calibrations as

$$\left\langle \frac{P^x}{P^{4.2}} \right\rangle \equiv \frac{1}{N_{\text{cl}}} \sum_{i=1}^{N_{\text{cl}}} \frac{P_i^x}{P_i^{4.2}} \quad (22)$$

where i denotes the value for each individual cluster, x refers to 3.1 or 4.1, and N_{cl} is the number of clusters used in the calculation.

Examples of the differences in the effective area for the different calibrations are shown in Figure 1 for both ACIS-I (CL0016+1609; top) and ACIS-S (MS1054.5-0321; bottom) observations of galaxy clusters. Shown are the effective areas (left) and fractional residuals from the 4.2 calibration (right) for the 3.1 (red), 4.1 (blue), and 4.2 (black) calibration versions. The vertical dotted lines denote the 0.7-7.0 keV energy range used in this analysis. Residuals are defined as $\Delta A/A^{4.2} = (A^x - A^{4.2})/A^{4.2}$, where x refers to 3.1 or 4.1. The same definition of residual applies to the other cluster properties with A replaced by the parameter of interest. The resulting temperatures follow the same trends as the normalization of the effective areas ($T_e \propto A(E)$).

The results from the Markov chain analysis are summarized in Table 4 for all three calibration versions. The basic trend is as expected from the calibration notes and the effective area curves, $T_e^{3.1} > T_e^{4.2} > T_e^{4.1}$. A2163 appears in the table twice. Following the methodology outlined above results in what seems like unrealistically high temperatures, 16 – 20 keV between the calibrations. In addition, the combination of its formally small uncertainties and it being very far from the mean inferred Hubble parameter (due to its high T_e) causes undue influence on the resultant Hubble parameter (see Section 4). This cluster is among a handful of clusters that are known to have H I column densities

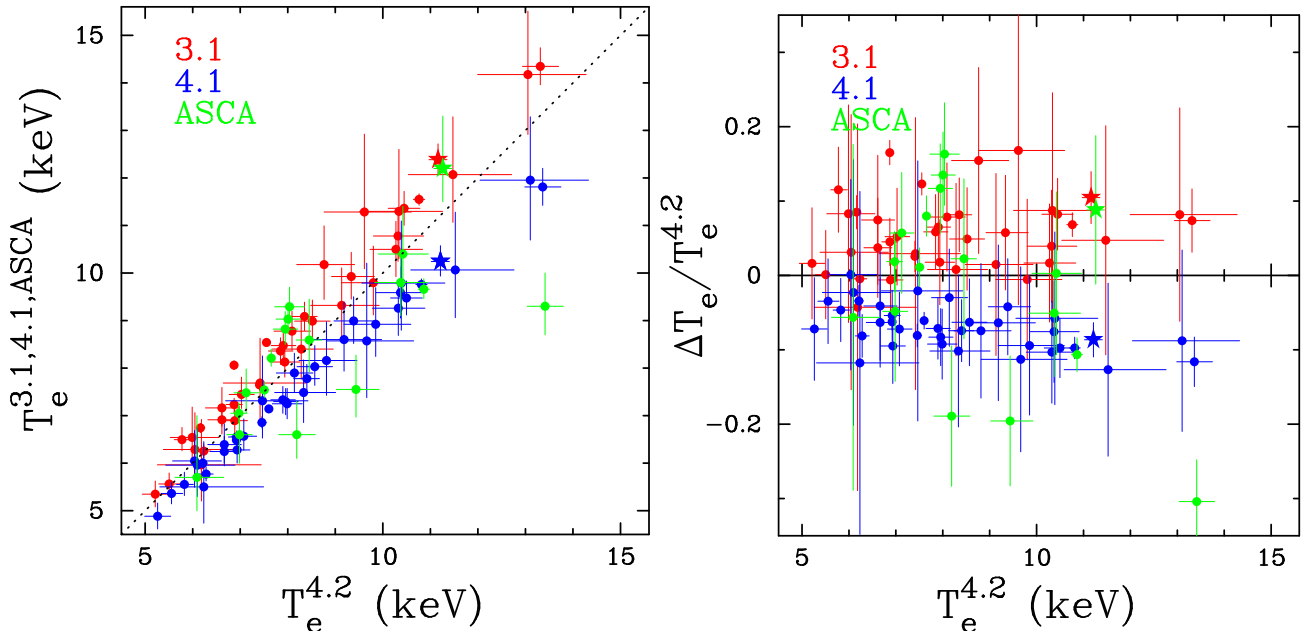


FIG. 2.— Comparison of different temperature measurements (left) and the corresponding fractional residuals from the 4.2 calibration results (right). Temperature determinations using the 3.1 calibration (red) and 4.1 (blue) calibration are compared against temperatures using the newest 4.2 version. Also plotted are the *ASCA* (green) temperatures adopted in R02 for comparison of the 17 clusters that overlap with this work. The dotted black line shows the equality relation. Residuals are defined as $\Delta T_e/T_e^{4.2} = (T_e^x - T_e^{4.2})/T_e^{4.2}$, where x is the 3.1 (red), 4.1 (blue), or *ASCA* (green) results. Error bars show 68% confidence statistical uncertainties and the A2163 results are denoted by stars. Points are slightly offset along the x -axis in both cases in order to make it easier to distinguish between the different calibrations.

that are significantly different from the Dickey & Lockman (1990) values (e.g., Govoni et al. 2004). When adopting the updated column density of $18.7 \times 10^{20} \text{ cm}^{-2}$ (Govoni et al. 2004) instead of the Dickey & Lockman (1990) value of $12.1 \times 10^{20} \text{ cm}^{-2}$ the temperatures and other parameters change significantly because the column density strongly affects the lower energy part of the spectrum. The updated temperatures are in the range 10 – 14 keV, placing A2163 more in line with previous results and closer to the mean Hubble constant from the other clusters, lessening the impact from this single cluster. As an aside, also note that a newer H I column density study yields an even lower value of $10.9 \times 10^{20} \text{ cm}^{-2}$ (Kalberla et al. 2005). Choosing an updated H I column density destroys our uniform, systematic study by treating one cluster special. It is tempting to throw out this cluster to keep the uniformity. We therefore present results for both the Dickey & Lockman (1990) and Govoni et al. (2004) N_{H} values and also explore the effects of removing A2163 from the sample. Initially A2163 has a large impact on the final H_0 value. However, once the new value of N_{H} is adopted, A2163 basically has no effect on the results. Table 4 shows the results for both column density values. The figures show results for only the adopted updated N_{H} value and a star is used to denote A2163 to distinguish it from the other clusters.

R02 adopted N_{H} values from spectral fits where available (five clusters), used the value from the Bell Labs H I survey (Stark et al. 1992) as adopted in a detailed analysis for that one cluster (Donahue et al. 1999), and adopted the DL values (Dickey & Lockman 1990) for the remaining clusters. In particular, the adopted value for A2163 is $N_{\text{H}} = 16.5 \times 10^{20} \text{ cm}^{-2}$ (Elbaz et al. 1995). A quick spectral fit to the *Chandra* data including N_{H} as a free parameter suggests $N_{\text{H}} \sim 16 \times 10^{20} \text{ cm}^{-2}$. Further investigation is beyond the scope of this work. We are concerned with the overall differences between calibrations more so than the values of the individual derived quantities for a particular cluster.

Figure 2 shows the comparison of the temperatures from the version 3.1 (red) and 4.1 (blue) calibration versus that of the 4.2 calibration (left) along with the fractional residuals compared to the 4.2 calibration results (right). Also plotted are the *ASCA* results (green) for the 17 overlapping clusters used for SZE/X-ray distances using the same SZE data as B06 but using *ROSAT* and *ASCA* data (R02). The dotted line shows the one-to-one correspondence. There is a clear division between the 3.1 and 4.1 results on either side of the equality line, with 3.1 falling above the relation and 4.1 falling below, clearly seen in the residuals. A2163 results are shown with stars.

The mean ratios between temperatures are

$$\left\langle \frac{T_e^{3.1}}{T_e^{4.2}} \right\rangle = 1.06 \pm 0.05, \quad \left\langle \frac{T_e^{4.1}}{T_e^{4.2}} \right\rangle = 0.93 \pm 0.03, \quad (23)$$

where the above uncertainty is simply the rms in the ratio. The changes between the two older calibrations and the newest are roughly the same order ($\sim 6\%$) but in different directions. Therefore, the average change in temperatures between the 3.1 and 4.1 calibrations is of order $\sim 12\%$, which would produce a $\sim 24\%$ difference in the inferred Hubble

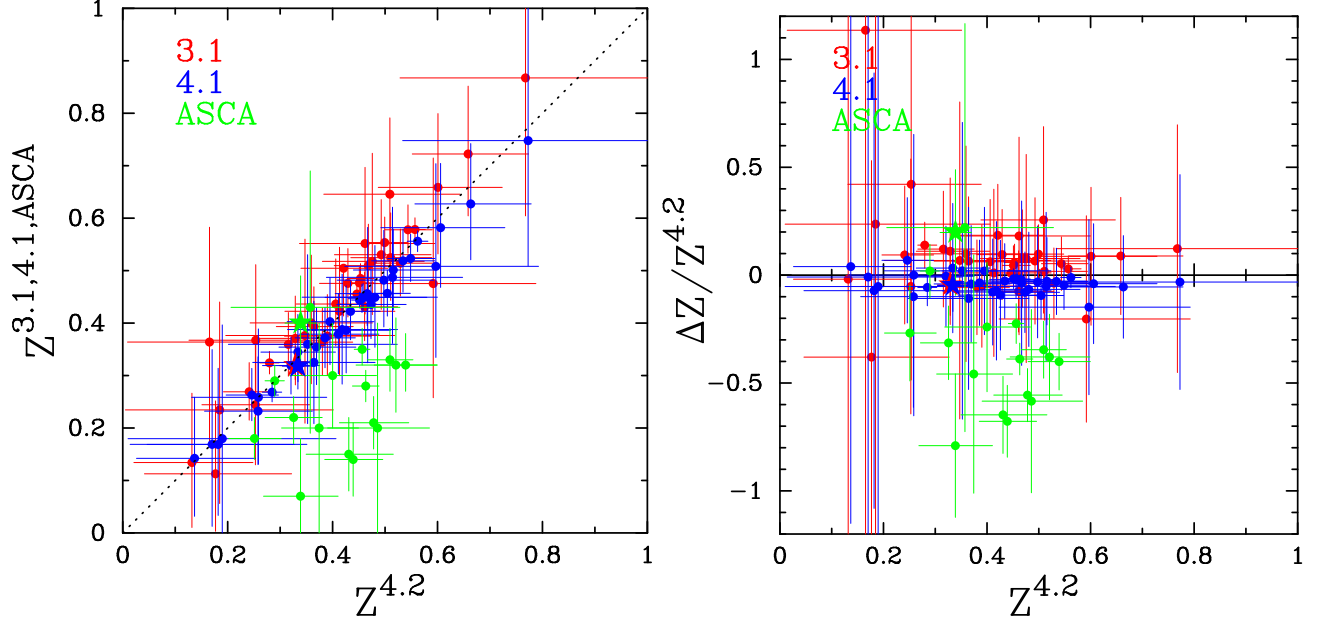


FIG. 3.— Comparison of different abundance measurements (left) and the corresponding fractional residuals from the 4.2 calibration results (right). Abundance determinations using the 3.1 calibration (red) and 4.1 (blue) calibration are compared against metallicities using the newest 4.2 version. Also plotted are the *ASCA* (green) abundances adopted in R02 for comparison of the 17 clusters that overlap with this work. The dotted black line shows the equality relation. Error bars show 68% confidence statistical uncertainties and the A2163 results are denoted by stars. Points are slightly offset along the x -axis in both cases in order to make it easier to distinguish between the different calibrations.

parameter.

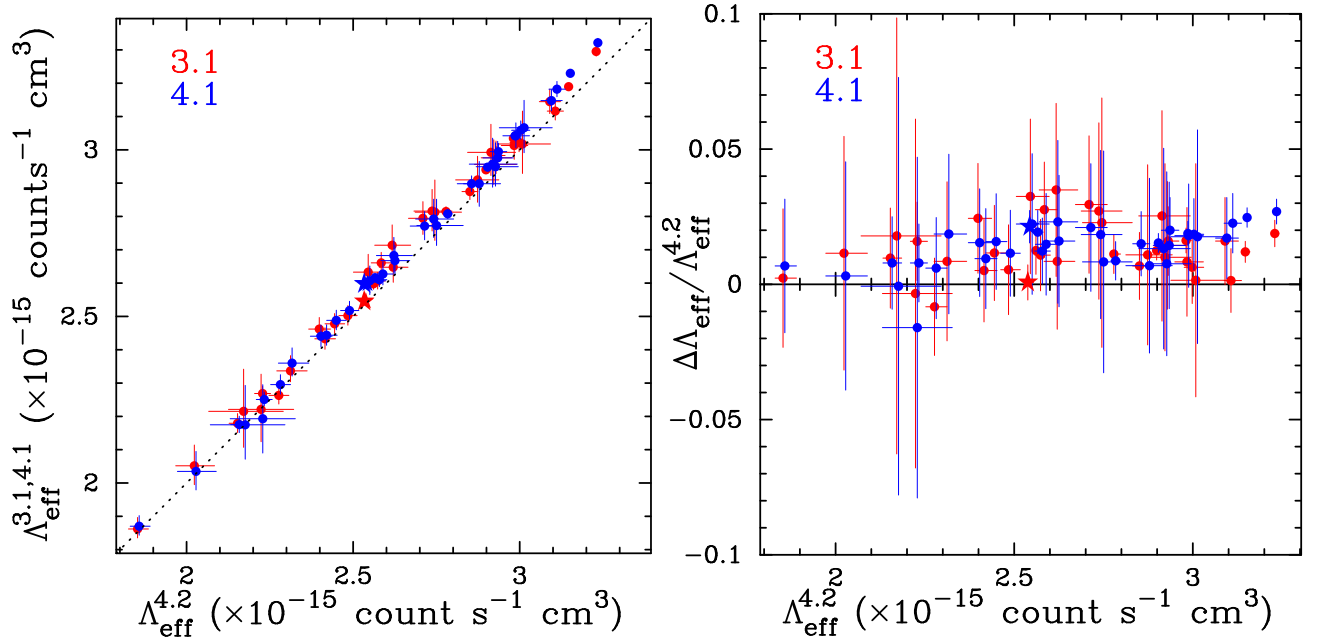


FIG. 4.— Comparison of different effective X-ray cooling functions (left) and the corresponding fractional residuals (right). Effective cooling function determinations using calibration versions 3.1 (red) and 4.1 (blue) are compared against emissivities using the new 4.2 calibration results. The dotted black line shows the equality relation. Error bars show 68% confidence statistical uncertainties and the A2163 results are denoted by stars. Points are slightly offset along the x -axis in both cases in order to make it easier to distinguish between the different calibrations.

The mean ratios comparing against the B06 results are

$$\left\langle \frac{T_e^{3.1}}{T_{eB06}} \right\rangle = 1.05 \pm 0.11, \quad \left\langle \frac{T_e^{4.1}}{T_{eB06}} \right\rangle = 0.92 \pm 0.10, \quad \left\langle \frac{T_e^{4.2}}{T_{eB06}} \right\rangle = 0.99 \pm 0.11. \quad (24)$$

Therefore it is likely that there is a small ($\sim 5\%$) overall systematic between the spectral analysis of B06 and this

TABLE 1
 COMPILATION OF MEAN RATIOS: UPDATED A2163 N_H

Parameter	3.1/4.2	4.1/4.2	3.1/B06	4.1/B06	4.2/B06	ASCA/4.2
T_e	1.06 ± 0.05	0.93 ± 0.03	1.05 ± 0.11	0.92 ± 0.10	0.99 ± 0.11	0.98 ± 0.12
Z	1.08 ± 0.21	0.96 ± 0.04	1.16 ± 0.43	1.03 ± 0.31	1.08 ± 0.34	0.66 ± 0.28
Λ_{eff}	1.01 ± 0.01	1.01 ± 0.01	1.03 ± 0.07	1.03 ± 0.07	1.02 ± 0.07	...
$f_{(\nu, T_e)}$	0.998 ± 0.002	1.002 ± 0.001	0.999 ± 0.003	1.003 ± 0.004	1.001 ± 0.003	...
$A(1\text{keV})^a$	1.01 ± 0.02	0.95 ± 0.01	0.96 ± 0.10	0.91 ± 0.10	0.95 ± 0.10	...
d_A^b	0.93 ± 0.08	1.13 ± 0.06	1.06 ± 0.24	1.29 ± 0.29	1.15 ± 0.25	1.07 ± 0.37

^a B06 are the effective areas from the 3.1 calibration using only those data sets that appear in Bonamente et al. 2006.

^b B06 are the published distances from Bonamente et al. 2006.

work. Given the various decisions on background regions, spectral extraction regions, and so forth, this is reasonable agreement. This analysis removes those uncertainties between analyses by performing the same systematic analysis on the same data for three different *Chandra* calibration versions. We focus on the differences between the calibrations rather than the values themselves. The mean ratios of the temperatures as well as other parameters considered here are summarized in Table 1.

The abundances from the spectral fits (left) and the fractional residuals with the 4.2 results (right) are plotted in Figure 3. Again calibration versions 3.1 (red) and 4.1 (blue) are plotted against the 4.2 calibration and the dotted line shows equality. Also shown are the *ASCA* abundances adopted in R02. There is no clear trend in the *Chandra* results as is the case for the temperatures. There is a mild offset between the *Chandra* and *ASCA* metallicities. The *ASCA* results are compiled from the literature and the data are not uniformly analyzed, the abundances used for the analyses often differing. The abundances do change the effective cooling functions, Λ_{eff} . However, the effects of metallicity on Λ_{eff} are small, typically on the order of $\sim 1\%$ and $\lesssim 5\%$ even for changing the abundance by factors of 2 or 3.

Derived effective cooling functions from the spectral analysis (left) and corresponding fractional residuals from the 4.2 calibration (right) are illustrated in Figure 4. Results for calibration versions 3.1 (red) and 4.1 (blue) are shown against that of version 4.2. The equality relation is also shown. There is a clear trend for Λ_{eff} to be greater in 3.1 and 4.1 compared to the 4.2 results but as shown by the residuals, it is a small effect, $< 4\%$ for 3.1 and $< 2\%$ for the 4.1 results.

The abundance of metals does not directly enter the distance calculation. However, it indirectly enters through the X-ray cooling function, Λ_{eff} . The X-ray temperature also indirectly enters the calculation through relativistic corrections to the frequency dependence of the SZE, $f_{(\nu, T_e)}$, where ν is the frequency of the observations (see Section 4). Mean ratios and rms's for the temperature, abundance, X-ray cooling function, SZE frequency function including relativistic corrections (Itoh et al. 1998), the effective area at 1 keV, and angular diameter distance (see Section 4) are summarized in Table 1.

4. IMPLICATIONS TO THE ESTIMATE OF H_0

Direct angular diameter distances, d_A , from a combined SZE and X-ray analysis are straight forward to compute, in theory, (see, for example Birkinshaw et al. 1991; Reese et al. 2002; Bonamente et al. 2006), particularly for the simple isothermal β -model. The actual observations and parameter extraction from the data are not as straight forward. We concern ourselves here with only the components of the distance calculation that involve X-ray spectral properties or are derived from them. SZE/X-ray derived distances have the following dependence on X-ray spectral properties

$$d_A \propto \frac{\Lambda_{\text{eff}}}{T_e^2 f_{(\nu, T_e)}^2 S_X} \propto \frac{\Lambda_{\text{eff}} A(E_{\text{fid}})}{T_e^2 f_{(\nu, T_e)}^2}, \quad (25)$$

where T_e is the electron temperature, Λ_{eff} is the effective X-ray cooling function (see Section 2.2), and $f_{(\nu, T_e)}$ is the spectral dependence of the SZE at frequency, ν , including relativistic corrections, which depend on T_e (e.g., Itoh et al. 1998; Challinor & Lasenby 1998), S_X is the X-ray surface brightness that depends on the effective area that changes between the calibrations, $A(E)$ is the effective area of the observatory, and we have used the fact that $S_X \propto \mathcal{N}_X/A(E_{\text{fid}})$, where \mathcal{N}_X is the number of observed counts and is constant. Since the exposure maps are all computed at 1 keV, S_X simply changes by the ratio of effective areas at $E_{\text{fid}} = 1$ keV. It is not immediately obvious how the spectral results will affect the final Hubble constant due to the complexity of the dependencies on spectral parameters. However, it is clear that a $\sim 10\%$ change in T_e will have an appreciable effect on the distances and therefore on the inferred Hubble constant.

Cluster spatial properties from β -model fits (B06) are adopted for the distance calculation. X-ray spectral properties from this analysis for the three calibrations are combined with the adopted cluster spatial properties in order to compute distances to each galaxy cluster. We estimate the uncertainty on d_A by backing out the X-ray spectral variable uncertainty from the published uncertainty and including the new *Chandra* calibration spectral result uncertainties

assuming everything adds in quadrature. Namely we compute the uncertainty in d_A by

$$\left(\frac{\delta d_A^x}{d_A^x}\right)^2 = \left(\frac{\delta d_A^{B06}}{d_A^{B06}}\right)^2 - 2\left(\frac{\delta T_e^{B06}}{T_e^{B06}}\right)^2 - \left(\frac{\delta \Lambda_{\text{eff}}^{B06}}{\Lambda_{\text{eff}}^{B06}}\right)^2 + 2\left(\frac{\delta T_e^x}{T_e^x}\right)^2 + \left(\frac{\delta \Lambda_{\text{eff}}^x}{\Lambda_{\text{eff}}^x}\right)^2, \quad (26)$$

where x refers to one of the three calibrations of this work and $B06$ refers to the published values (B06). The average of the positive and negative uncertainties is used for the uncertainty. This method preserves, as best we can, the correlations among the parameters. In particular, r_c and β from the β -model are strongly correlated (for an example in this context see Reese et al. 2000). However, the spectral results are independent of the β -model. Therefore we can preserve this correlation through uncertainty propagation with this method. The temperature uncertainty comes with a factor of 2 because the angular diameter distance is inversely proportional to temperature squared, $d_A \propto T_e^{-2}$. We include the additional sources of statistical uncertainty, $\sim 19\%$, from Table 3 of B06 by adding in quadrature to the uncertainties computed from Equation (26). These total statistical uncertainties are then used for the H_0 calculation and are summarized in Table 4, which shows the derived angular diameter distances with 68% statistical uncertainties.

The Hubble constant is computed by performing a χ^2 fit to the cluster distances using the theoretical angular diameter distance relation for a flat, Λ -dominated universe with $\Omega_\Lambda = 0.73$ and $\Omega_m = 0.27$ consistent with the *WMAP* results (Komatsu et al. 2010, 2009). The resulting angular diameter distances for the full sample and updated N_H for A2163 yield

$$H_0^{3.1} = 70.0 \pm 3.7 \text{ km s}^{-1} \text{ Mpc}^{-1}, \quad (27)$$

$$H_0^{4.1} = 55.4 \pm 2.9 \text{ km s}^{-1} \text{ Mpc}^{-1}, \quad (28)$$

$$H_0^{4.2} = 63.7 \pm 3.3 \text{ km s}^{-1} \text{ Mpc}^{-1}, \quad (29)$$

where the uncertainties are statistical only at 68% confidence with $\chi^2 = 40.6, 34.4, 38.8$ for 37 degrees of freedom for the 3.1, 4.1, and 4.2 calibrations respectively. Solely from the changing calibration, taking the 4.2 calibration as the baseline, $H_0^{3.1}/H_0^{4.2} = 1.10$ and $H_0^{4.1}/H_0^{4.2} = 0.87$, showing changes of roughly 10% and 13% in the determination of the Hubble constant, respectively. There is a $\sim 23\%$ change in H_0 between the 3.1 and 4.1 calibrations, consistent with the expectation from the mean of the ratio of temperatures (see Section 3.3 and Table 1).

In Figure 5, we plot the angular diameter distances (top) and corresponding Hubble constants (bottom) determined using the results from the 3.1 (red), 4.1 (blue), and 4.2 (black) calibrations for each cluster. In both cases, the right panels show the fractional residuals from the 4.2 calibration results. Results from R02 are also plotted for comparison and denoted as *ASCA* (green). The best-fit theoretical angular diameter distance relations (top) and corresponding Hubble constants (bottom) are also shown. Angular diameter distances are also summarized in Table 4 for each of the calibrations. Uncertainties are 68% confidence and include both the uncertainty from the fit and the additional sources of statistical uncertainty from Table 3 of B06. In general, the distances follow the trends expected from the temperatures, namely, $d_A^{3.1} < d_A^{4.2} < d_A^{4.1}$, indicating that the temperature changes dominate the changes in distances.

Hubble parameters are computed from the determined angular diameter distances using χ^2 for the original $N_H = 12.1 \times 10^{20} \text{ cm}^{-2}$ for A2163, the updated A2163 N_H , and excluding A2163 from the fit for each of the three calibrations. The results are compiled in Table 2, where the uncertainties are 68% confidence statistical uncertainties and the number in parentheses is the χ^2 at the best-fit value. Hubble parameters are computed from χ^2 fits for the 17 clusters that overlap in the R02 sample, becoming 16 clusters when A2163 is excluded. A simple average is also computed for each case by first converting the d_A for each cluster into a Hubble parameter and then averaging. Finally, a χ^2 fit is done for the published values of B06 and R02 both including and excluding A2163.

Table 2 summarizes the full set of Hubble parameter estimates. The beginning of each section marks the H_0 estimation method (χ^2 or average) followed by the number of clusters used in each calculation. The last two sections are the results of performing χ^2 fits both including and not including A2163 using the published distances from B06 and R02. In the case of R02, the first entry includes the entire sample of 18 clusters although only 17 of which overlap with the B06 sample. A fit of just those 17 appears in the second column and then the results without A2163 in the third column.

Using the means of the ratios of the X-ray spectral parameters with respect to the calibration version 4.2 results (Table 1) and scaling $H_0^{4.2}$ implies $H_0^{3.1} = 69.2 \text{ km s}^{-1} \text{ Mpc}^{-1}$ and $H_0^{4.1} = 56.5 \text{ km s}^{-1} \text{ Mpc}^{-1}$, very close to the Hubble parameters from the χ^2 analysis. This is also true when dropping A2163 from the analysis but not true when using the Dickey & Lockman (1990) N_H value for A2163. In that case, using the ratios to scale the 4.2 results predicts $H_0^{3.1} = 75.5 \text{ km s}^{-1} \text{ Mpc}^{-1}$ and $H_0^{4.1} = 62.3 \text{ km s}^{-1} \text{ Mpc}^{-1}$ compared to the χ^2 results 82.8 and 58.4 $\text{km s}^{-1} \text{ Mpc}^{-1}$, respectively.

5. DISCUSSION

We perform a uniform, systematic spectral analysis of 38 galaxy clusters using three different *Chandra* calibrations and find significant differences in the inferred spectral properties of galaxy clusters between the calibrations. Using the newest calibration, 4.2, as the baseline to which to compare, the temperatures change $\sim 6\%$ on average in the 3.1 and 4.1 calibrations, but in opposite directions. In particular, the temperature changes between the extreme cases (3.1 and 4.1) show a $\sim 13\%$ difference in T_e , on average. These results are consistent with an analysis of 10 galaxy clusters that found the 4.1 calibration results yield $\sim 10\%$ lower temperatures than the 3.1 calibration (Gaetz 2009).

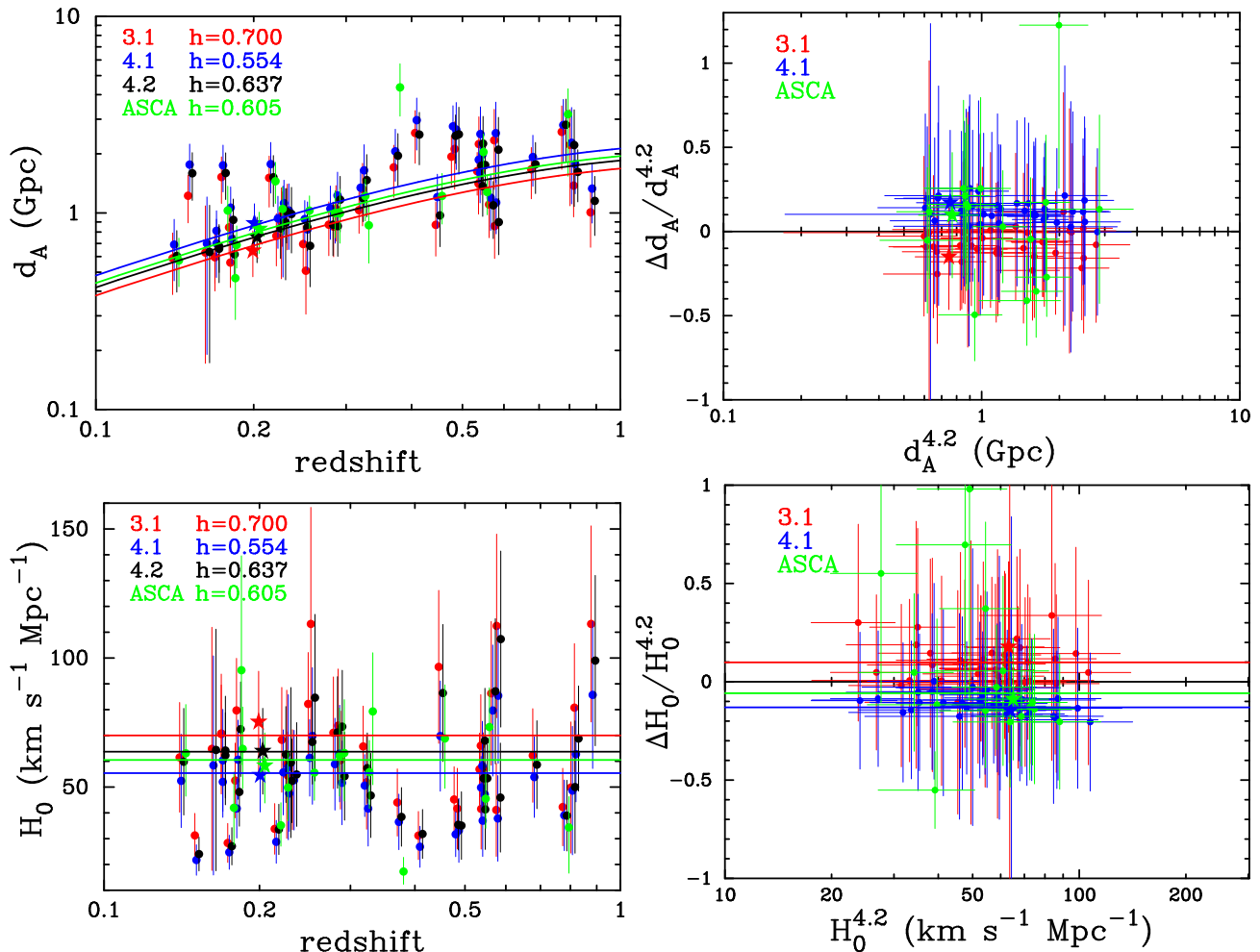


FIG. 5.— Angular diameter distances (top) and corresponding Hubble parameters (bottom) determined using the results from the 3.1 (red), 4.1 (blue), and 4.2 (black) calibrations. In both cases, the right panels show the fractional residuals from the 4.2 calibration results. Results from R02 are also plotted for comparison and denoted as *ASCA* (green). The best-fit theoretical angular diameter distance relations are also shown for each calibration (top, left) with corresponding Hubble parameters in the legend. The best-fit Hubble parameters are shown in the H_0 figure (bottom, left) and corresponding residuals (bottom, right). Error bars show 68% confidence statistical uncertainties and the A2163 results are denoted by stars. Points are offset slightly along the x -axis in order to make it easier to distinguish between the different calibrations.

The differences in spectral properties of galaxy clusters between the calibrations may have profound implications on inferred cosmological parameters from galaxy cluster studies.

Using the simple isothermal β -model as a vehicle we explore the ramifications of the effects of the *Chandra* calibration on a particular cosmological application, distances to galaxy clusters from a combined analysis of SZE and X-ray data. Because $H_0 \propto T_e^2$, changes in cluster temperatures have a potentially large impact on the inferred Hubble parameter. The 3.1, 4.1, and 4.2 calibrations imply Hubble constants of 70.0, 55.4, and 63.7 $\text{km s}^{-1} \text{Mpc}^{-1}$ using the updated column density for A2163 results. The results remain essentially unchanged when removing A2163 from the sample to preserve the uniformity of the analysis to the last detail. Simply from the effects of the *Chandra* calibration, the 3.1 results yield a 10% higher H_0 than the most recent 4.2 calibration and the 4.1 results yield a 13% lower H_0 than the 4.2 calibration results. This is in rough agreement with what the mean ratios of temperatures would predict, 13% and 14% effects for the 3.1 and 4.1 calibrations, respectively. This strongly suggests that, although there are a number of quantities that change with the spectral results, the change in T_e is, by far, the most important when considering SZE/X-ray derived distance based estimates of the Hubble parameter. In the most extreme case, comparing the 3.1 to the 4.1 results, there is a $\sim 24\%$ change in the Hubble parameter due to the change in *Chandra* calibration.

Although the isothermal assumption is over-simplistic, it is sufficient to study the effects of the new calibration on SZE/X-ray derived distances. B06 showed that the Hubble parameter estimates from SZE/X-ray distances do not depend as strongly on the model as one might naively believe. In particular, the isothermal β -model yields results consistent with the more sophisticated hydrostatic equilibrium model and an isothermal β -model with the central regions of the X-ray data removed that they considered. This simple isothermal β -model also facilitates isolating the effects that the different spectral parameters have on the distances and therefore on the Hubble constant.

SZE/X-ray distances tend to favor a Hubble constant of order 60 $\text{km s}^{-1} \text{Mpc}^{-1}$ (e.g., Carlstrom et al. 2002;

TABLE 2
COMPILATION OF H_0 RESULTS

H_0	DL A2163 N_H	Updated A2163 N_H	No A2163
χ^2 full sample	38	38	37
$H_0^{3.1}$	$82.8 \pm 4.6(75.9)$	$70.0 \pm 3.7(40.6)$	$69.7 \pm 3.7(40.5)$
$H_0^{4.1}$	$58.4 \pm 3.1(42.4)$	$55.4 \pm 2.9(34.3)$	$55.5 \pm 2.9(34.3)$
$H_0^{4.2}$	$68.8 \pm 3.7(52.2)$	$63.7 \pm 3.3(38.8)$	$63.7 \pm 3.4(38.8)$
χ^2 R02 overlap	17	17	16
$H_0^{3.1}$	$90.1 \pm 7.0(48.5)$	$66.9 \pm 4.7(15.8)$	$66.1 \pm 4.8(15.5)$
$H_0^{4.1}$	$58.2 \pm 4.1(21.2)$	$52.3 \pm 3.6(11.8)$	$52.2 \pm 3.8(11.8)$
$H_0^{4.2}$	$70.1 \pm 5.1(28.7)$	$60.5 \pm 4.3(14.4)$	$60.2 \pm 4.4(14.3)$
Avg full sample	38	38	37
$H_0^{3.1}$	66.1 ± 30.3	62.9 ± 21.7	62.6 ± 21.9
$H_0^{4.1}$	52.5 ± 17.2	51.3 ± 15.4	51.2 ± 15.6
$H_0^{4.2}$	59.7 ± 22.1	58.0 ± 18.9	57.8 ± 19.1
Avg R02 overlap	17	17	16
$H_0^{3.1}$	68.3 ± 36.1	61.2 ± 17.6	60.4 ± 17.7
$H_0^{4.1}$	51.8 ± 16.9	49.2 ± 12.0	48.9 ± 12.3
$H_0^{4.2}$	60.0 ± 23.3	56.1 ± 15.5	55.6 ± 15.9
χ^2 B06 refit	38		37
H_0^{B06}	$76.2 \pm 4.1(55.9)$...	$73.5 \pm 4.1(51.7)$
χ^2 R02 refit	18	17	16
H_0^{R02}	$60.8 \pm 4.0(16.5)$	$60.5 \pm 4.1(16.4)$	$60.7 \pm 4.3(16.4)$

NOTE. — DL is the Dickey & Lockman (1990) H I survey. The first row of each section describes the type of H_0 calculation (χ^2 or average) followed by the number of clusters used in the fit for each of the three cases considered. The numbers in parentheses are the χ^2 value at the best fit. The last two sections are fits to the published B06 and R02 distances. For R02, the first column is the full sample of R02, the second column include the 17 overlapping clusters with this work, and the third column then also excludes A2163 from the χ^2 fit.

Reese et al. 2002) with a few exceptions (e.g., Bonamente et al. 2006; Mason et al. 2001). This is in contrast to other probes that favor $H_0 \sim 70 \text{ km s}^{-1} \text{ Mpc}^{-1}$, such as the *HST* H_0 key project (Freedman et al. 2001), recent supernova results (e.g., Hicken et al. 2009), and recent *WMAP* results (Komatsu et al. 2009, 2010). Potential systematics in SZE/X-ray derived estimates of H_0 are still formidable (see for example, Birkinshaw et al. 1991; Hughes & Birkinshaw 1998; Reese et al. 2002; Bonamente et al. 2006), making the results consistent within the uncertainties. It is still curious that SZE/X-ray distances tend to favor a lower Hubble constant.

One possible explanation of this bias in H_0 from SZE/X-ray determined distances to galaxy clusters is the combined effects from the degree of inhomogeneity and the multi-temperature structure of the ICM (Kawahara et al. 2008a). The bias vanishes in the limit of an isothermal and homogeneous ICM, an idealized and unrealistic limit. The presence of inhomogeneity in the cluster gas is suggested by a detailed study of the nearby galaxy cluster A3667 (Kawahara et al. 2008b), which finds 30%–40% rms density fluctuations in that cluster. In addition, 20% rms temperature fluctuations have been seen in Hydra A (Simionescu et al. 2009). The theoretical underpinning of the inhomogeneity model was boosted because the nearby galaxy cluster A3667 exhibits the expected lognormal signature (Kawahara et al. 2008b).

This model implies that the bias in the Hubble constant can be decomposed into three factors

$$f_H \equiv \frac{H_{0,\text{est}}}{H_{0,\text{true}}} = \chi_\sigma \chi_T(T_{\text{ew}}) \frac{\chi_T(T_{\text{spec}})}{\chi_T(T_{\text{ew}})}. \quad (30)$$

where χ_σ , $\chi_T(T_{\text{ew}})$, and $\chi_T(T_{\text{spec}})/\chi_T(T_{\text{ew}})$ represent the systematic errors due to the presence of ICM gas inhomogeneities, non-isothermality, and the difference between the spectroscopic (T_{spec}), and emission-weighted (T_{ew}) temperatures. Numerical values for each of the above bias factors, of course, depend crucially on the degree of inhomogeneities and the temperature structure of the ICM. However, simulated clusters suggest that these biases are roughly (10–30)% overestimate, (0–20)% underestimate, and (10–20)% underestimate, respectively, resulting in an overall (10–20)% underestimate in the Hubble parameter. For analytic expressions and further details, see Kawahara et al. (2008a).

We note that the above result is consistent with the many studies of the statistical and systematic uncertainties in Hubble constant determinations from SZE/X-ray distances (e.g., Inagaki et al. 1995; Kobayashi et al. 1996; Yoshikawa et al. 1998; Hughes & Birkinshaw 1998; Sulkanen 1999; Wang & Fan 2006) that find only small biases if any at all. All of these studies use an emission-weighted temperature for the simulated clusters. This corresponds to neglecting the third factor in Equation (30), and thus leading to no substantial bias because the first and second factors coincidentally compensate each other. Mazzotta et al. (2004) are the first to point out clearly that the spectroscopic temperature, T_{spec} , is systematically lower than the emission-weighted temperature, T_{ew} (see also Mathiesen & Evrard

2001; Rasia et al. 2005), so that the third factor in Equation (30) is essential (Kawahara et al. 2007, 2008a).

This bias can theoretically be accounted for with more realistic models of the ICM. For example, once the variance of the ICM inhomogeneity is known, a fit to even a simplistic model for the temperature profile largely avoids the bias in H_0 from SZE/X-ray distances (Kawahara et al. 2008a). Progress on this front will require a multi-wavelength approach combining recent SZE experiments, deep X-ray observations, and weak lensing measurements.

The large potential systematics in SZE/X-ray derived distances and inferred Hubble constant means that the various results are consistent with each other and other probes of H_0 (for detail of the systematics, see, e.g., Reese et al. 2002; Bonamente et al. 2006). Here, we took a detailed look at one of those systematics, the effect of the *Chandra* calibration on cluster temperatures. There have been very little work on including calibration uncertainties in X-ray analysis. However, a Monte Carlo approach to incorporate calibration uncertainty for parameter estimation from *Chandra* ACIS-S observations has been developed (Drake et al. 2006). Better methods of incorporating uncertainties, especially systematics such as instrumental calibration, will need to be developed.

There are alternative methods to X-ray spectroscopy for determining galaxy cluster temperatures. Theoretical studies of non-parametric deprojection methods of SZE and X-ray imaging data on both idealized and simulated clusters suggest that cluster temperature profiles may be accurately reconstructed without X-ray spectroscopy (Yoshikawa & Suto 1999; Puchwein & Bartelmann 2006; Ameglio et al. 2007). Both parametric and non-parametric methods applied to actual SZE and X-ray data also show broad agreement with temperature profiles derived from X-ray spectroscopy (Kitayama et al. 2004; Nord et al. 2009; Mroczkowski et al. 2009). Cluster temperatures may also be inferred from SZE data only if one assumes the value for the gas mass fraction of the cluster (LaRoque et al. 2006; Joy et al. 2001). Because these methods use only X-ray imaging data, they do not require the longer exposure times necessary for spectroscopic T_e measurements. In addition, these alternative temperature measurements may, in theory, alleviate some of the dependence of derived cosmological parameters on the *Chandra* calibration. However, most methods currently have large uncertainties on the cluster temperature and are complicated by the fact that they still depend on the *Chandra* (or other X-ray observatory) calibration through the effective area for both exposure maps and the cooling function calculation.

The determination of galaxy cluster temperatures is particularly important because it is widely used to infer the gravitational mass of clusters. Potential systematics on cluster temperatures will have a strong impact on cosmological parameters when using clusters as probes of cosmology. In particular, temperature systematics will strongly affect the normalization of the matter power spectrum, σ_8 , through the cluster temperature–halo mass relation in conjunction with cluster abundances (e.g., Rasia et al. 2005; Shimizu et al. 2006).

Analysis of observations of galaxy clusters does have the potential to provide insight into cosmology and has been successful in the past, favoring low Ω_M long before hints of a cosmological constant appeared (e.g., White et al. 1993). Surveys of galaxy clusters have the tantalizing appeal that they probe the growth of structure, one of the few probes to do so, and have the potential to constrain tightly the equation of state of the dark energy (e.g., Bartlett & Silk 1994; Holder et al. 2000; Haiman et al. 2001; Majumdar & Mohr 2004). However, in order to realize that potential, both galaxy clusters themselves and the details of the instruments must be understood precisely which will be feasible with combined efforts from ongoing observations and planned missions and observatories covering a wide range of wavelengths.

We are grateful to Akio Hoshino and Yoshitaka Ishisaki for useful discussions about the *Chandra* calibration that helped to motivate this work. We thank John Carlstrom, Massimiliano Bonamente, and Marshall Joy for a careful reading and comments on a draft of this manuscript. We are indebted to the *Chandra* help desk and calibration teams for answering many questions about the details of the *Chandra* calibration. This research has made extensive use of data obtained from the *Chandra* Data Archive and software provided by the *Chandra* X-ray Center (CXC). E.D.R. gratefully acknowledges support from a JSPS Postdoctoral Fellowship for Foreign Researchers (P07030). Y.S. acknowledges the support from the Global Scholars Program of Princeton University, and thanks people in Peyton Hall, Princeton University, for their warm hospitality and discussions. This work is supported by Grant-in-Aid for Scientific research of Japanese Ministry of Education, Culture, Sports, Science and Technology (Nos. 18740112, 18072002, 20-08324, 20-10466, 20340041, 22-5467, and 21740139), and by JSPS (Japan Society for Promotion of Science) Core-to-Core Program “International Research Network for Dark Energy”.

REFERENCES

- Allen, S. W., Rapetti, D. A., Schmidt, R. W., Ebeling, H., Morris, R. G., & Fabian, A. C. 2008, *MNRAS*, 383, 879
- Allen, S. W., Schmidt, R. W., Ebeling, H., Fabian, A. C., & van Speybroeck, L. 2004, *MNRAS*, 353, 457
- Ameglio, S., Borgani, S., Pierpaoli, E., & Dolag, K. 2007, *MNRAS*, 382, 397
- Arnaud, K. A. 1996, in *ASP Conf. Ser. 101, Astronomical Data Analysis Software and Systems V*, ed. G. H. Jacoby & J. Barnes (San Francisco, CA:ASP), 17
- Bahcall, N. A., Fan, X., & Cen, R. 1997, *ApJ*, 485, L53
- Balucinska-Church, M. & McCammon, D. 1992, *ApJ*, 400, 699
- Bartlett, J. G. & Silk, J. 1994, *ApJ*, 423, 12
- Birkinshaw, M. 1979, *MNRAS*, 187, 847
- . 1999, *Phys. Rep.*, 310, 97
- Birkinshaw, M., Hughes, J. P., & Arnaud, K. A. 1991, *ApJ*, 379, 466
- Bonamente, M., Joy, M. K., Carlstrom, J. E., Reese, E. D., & LaRoque, S. J. 2004, *ApJ*, 614, 56
- Bonamente, M., Joy, M. K., LaRoque, S. J., Carlstrom, J. E., Reese, E. D., & Dawson, K. S. 2006, *ApJ*, 647, 25
- Borgani, S., Rosati, P., Tozzi, P., Stanford, S. A., Eisenhardt, P. R., Lidman, C., Holden, B., Della Ceca, R., Norman, C., & Squires, G. 2001, *ApJ*, 561, 13
- Carlstrom, J. E., et al, A. A., & Vieira, K. V. J. D. 2009, arXiv:0907.4445
- Carlstrom, J. E., Holder, G. P., & Reese, E. D. 2002, *ARA&A*, 40, 643
- Cash, W. 1979, *ApJ*, 228, 939

- Cavaliere, A., Danese, L., & de Zotti, G. 1977, *ApJ*, 217, 6
- Cavaliere, A. & Fusco-Femiano, R. 1976, *A&A*, 49, 137
- . 1978, *A&A*, 70, 677
- Challinor, A. & Lasenby, A. 1998, *ApJ*, 499, 1
- David, L. P., Jones, C., & Forman, W. 1995, *ApJ*, 445, 578
- Dickey, J. M. & Lockman, F. J. 1990, *ARA&A*, 28, 215
- Donahue, M., Voit, G. M., Scharf, C. A., Gioia, I. M., Mullis, C. R., Hughes, J. P., & Stocke, J. T. 1999, *ApJ*, 527, 525
- Dorman, B. & Arnaud, K. A. 2001, in *Astronomical Society of the Pacific Conference Series*, Vol. 238, *Astronomical Data Analysis Software and Systems X*, ed. F. R. Harnden Jr., F. A. Primini, & H. E. Payne, 415
- Drake, J. J., Ratzlaff, P., Kashyap, V., Edgar, R., Izem, R., Jerius, D., Siemiginowska, A., & Vikhlinin, A. 2006, *Proc. SPIE*, 6270, 49
- Eke, V. R., Cole, S., & Frenk, C. S. 1996, *MNRAS*, 282, 263
- Eke, V. R., Cole, S., Frenk, C. S., & Patrick Henry, J. 1998, *MNRAS*, 298, 1145
- Elbaz, D., Arnaud, M., & Böhringer, H. 1995, *A&A*, 293, 337
- Ettori, S. & Fabian, A. C. 1999, *MNRAS*, 305, 834
- Ettori, S., Tozzi, P., & Rosati, P. 2003, *A&A*, 398, 879
- Evrard, A. E. 1997, *MNRAS*, 292, 289
- Feldman, U. 1992, *Phys. Scr.*, 46, 202
- Fowler, J. W., et al. 2010, arXiv:1001.2934
- Fowler, J. W., et al. 2007, *Appl. Opt.*, 46, 3444
- Freedman, W. L., et al. 2001, *ApJ*, 553, 47
- Gaetz, T. 2009, in *IACHEC*, <http://www.iachec.org/meetings/2009/index.html>
- Geweke, J. 1992, in *Bayesian Statistics IV*, ed. J. M. B. et al. (Oxford: Clarendon), 169
- Govoni, F., Markevitch, M., Vikhlinin, A., van Speybroeck, L., Ferretti, L., & Giovannini, G. 2004, *ApJ*, 605, 695
- Grego, L., Carlstrom, J. E., Reese, E. D., Holder, G. P., Holzzapfel, W. L., Joy, M. K., Mohr, J. J., & Patel, S. 2001, *ApJ*, 552, 2
- Gunn, J. E. 1978, in *Saas-Fee Advanced Course 8: Observational Cosmology Advanced Course*, ed. A. Maeder, L. Martinet, & G. Tammann, 1
- Haiman, Z., Mohr, J. J., & Holder, G. P. 2001, *ApJ*, 553, 545
- Henry, J. P. 2004, *ApJ*, 609, 603
- Henry, J. P. & Arnaud, K. A. 1991, *ApJ*, 372, 410
- Hicken, M., Wood-Vasey, W. M., Blondin, S., Challis, P., Jha, S., Kelly, P. L., Rest, A., & Kirshner, R. P. 2009, *ApJ*, 700, 1097
- Hincks, A. D., et al. 2009, arXiv:0907.0461
- Holder, G. P., Mohr, J. J., Carlstrom, J. E., Evrard, A. E., & Leitch, E. M. 2000, *ApJ*, 544, 629
- Hughes, J. P. & Birkinshaw, M. 1998, *ApJ*, 501, 1
- Inagaki, Y., Sugihara, T., & Suto, Y. 1995, *PASJ*, 47, 411
- Itoh, N., Kohyama, Y., & Nozawa, S. 1998, *ApJ*, 502, 7
- Ivezic, Z., Tyson, J. A., Allsman, R., Andrew, J., Angel, R., & for the LSST Collaboration. 2008, arXiv:0805.2366
- Joy, M., LaRoque, S., Grego, L., Carlstrom, J. E., Dawson, K., Ebeling, H., Holzzapfel, W. L., Nagai, D., & Reese, E. D. 2001, *ApJ*, 551, L1
- Kaiser, N. 2004, in *Society of Photo-Optical Instrumentation Engineers (SPIE) Conference Series*, Vol. 5489, *Society of Photo-Optical Instrumentation Engineers (SPIE) Conference Series*, ed. J. M. Oschmann Jr., 11
- Kalberla, P. M. W., Burton, W. B., Hartmann, D., Arnal, E. M., Bajaja, E., Morras, R., & Pöppel, W. G. L. 2005, *A&A*, 440, 775
- Kawahara, H., Kitayama, T., Sasaki, S., & Suto, Y. 2008a, *ApJ*, 674, 11
- Kawahara, H., Reese, E. D., Kitayama, T., Sasaki, S., & Suto, Y. 2008b, *ApJ*, 687, 936
- Kawahara, H., Suto, Y., Kitayama, T., Sasaki, S., Shimizu, M., Rasia, E., & Dolag, K. 2007, *ApJ*, 659, 257
- Kitayama, T., Komatsu, E., Ota, N., Kuwabara, T., Suto, Y., Yoshikawa, K., Hattori, M., & Matsuo, H. 2004, *PASJ*, 56, 17
- Kitayama, T. & Suto, Y. 1996, *ApJ*, 469, 480
- . 1997, *ApJ*, 490, 557
- Kobayashi, S., Sasaki, S., & Suto, Y. 1996, *PASJ*, 48, L107
- Komatsu, E., et al. 2009, *ApJS*, 180, 330
- Komatsu, E., et al. 2010, arXiv:1001.4538
- LaRoque, S. J., Bonamente, M., Carlstrom, J. E., Joy, M. K., Nagai, D., Reese, E. D., & Dawson, K. S. 2006, *ApJ*, 652, 917
- Lueker, M., et al. 2010, *ApJ*, 719, 1045
- Majumdar, S. & Mohr, J. J. 2004, *ApJ*, 613, 41
- Mantz, A., Allen, S. W., Ebeling, H., & Rapetti, D. 2008, *MNRAS*, 387, 1179
- Mantz, A., Allen, S. W., Rapetti, D., & Ebeling, H. 2010, *MNRAS*, 406, 1759
- Mason, B. S., Myers, S. T., & Readhead, A. C. S. 2001, *ApJ*, 555, L11
- Mathiesen, B. F. & Evrard, A. E. 2001, *ApJ*, 546, 100
- Mazzotta, P., Rasia, E., Moscardini, L., & Tormen, G. 2004, *MNRAS*, 354, 10
- Miyazaki, S., et al. 2006, *Proc. SPIE*, 6269, 9
- Mohr, J. J., Mathiesen, B., & Evrard, A. E. 1999, *ApJ*, 517, 627
- Mroczkowski, T., et al. 2009, *ApJ*, 694, 1034
- Myers, S. T., Baker, J. E., Readhead, A. C. S., Leitch, E. M., & Herbig, T. 1997, *ApJ*, 485, 1
- Neumann, D. M. & Böhringer, H. 1997, *MNRAS*, 289, 123
- Nord, M., et al. 2009, *A&A*, 506, 623
- Pen, U.-L. 1997, *New Astronomy*, 2, 309
- Predehl, P., et al. 2006, 6266, 36
- Predehl, P., et al. 2007, *Proc. SPIE* 6686, 19
- Puchwein, E. & Bartelmann, M. 2006, *A&A*, 455, 791
- Rasia, E., Mazzotta, P., Borgani, S., Moscardini, L., Dolag, K., Tormen, G., Diaferio, A., & Murante, G. 2005, *ApJ*, 618, L1
- Raymond, J. C. & Smith, B. W. 1977, *ApJS*, 35, 419
- Reese, E. D., Carlstrom, J. E., Joy, M., Mohr, J. J., Grego, L., & Holzzapfel, W. L. 2002, *ApJ*, 581, 53
- Reese, E. D., Mohr, J. J., Carlstrom, J. E., Joy, M., Grego, L., Holder, G. P., Holzzapfel, W. L., Hughes, J. P., Patel, S. K., & Donahue, M. 2000, *ApJ*, 533, 38
- Reichardt, C. L., et al. 2009, *ApJ*, 701, 1958
- Reiprich, T. H. & Böhringer, H. 2002, *ApJ*, 567, 716
- Rephaeli, Y. 1995, *ApJ*, 445, 33
- Rozo, E., et al. 2010, *ApJ*, 708, 645
- Sasaki, S. 1996, *PASJ*, 48, L119
- Schuecker, P., Böhringer, H., Collins, C. A., & Guzzo, L. 2003, *A&A*, 398, 867
- Shimizu, M., Kitayama, T., Sasaki, S., & Suto, Y. 2006, *PASJ*, 58, 291
- Silk, J. & White, S. D. M. 1978, *ApJ*, 226, L103
- Simionescu, A., Werner, N., Böhringer, H., Kaastra, J. S., Finoguenov, A., Brügggen, M., & Nulsen, P. E. J. 2009, *A&A*, 493, 409
- Squires, G., Neumann, D. M., Kaiser, N., Arnaud, M., Babul, A., Böhringer, H., Fahlman, G., & Woods, D. 1997, *ApJ*, 482, 648
- Stark, A. A., Gammie, C. F., Wilson, R. W., Bally, J., Linke, R. A., Heiles, C., & Hurwitz, M. 1992, *ApJS*, 79, 77
- Sulkanen, M. E. 1999, *ApJ*, 522, 59
- Sunyaev, R. A. & Zeldovich, I. B. 1980, *ARA&A*, 18, 537
- Sunyaev, R. A. & Zeldovich, Y. B. 1970, *Comments Astrophys. Space Phys.*, 2, 66
- . 1972, *Comments Astrophys. Space Phys.*, 4, 173
- Viana, P. T. P. & Liddle, A. R. 1996, *MNRAS*, 281, 323
- Vikhlinin, A., et al. 2009, *ApJ*, 692, 1060
- Wang, Y. & Fan, Z. 2006, *ApJ*, 643, 630
- White, D. A. & Fabian, A. C. 1995, *MNRAS*, 273, 72
- White, S. D. M., Navarro, J. F., Evrard, A. E., & Frenk, C. S. 1993, *Nature*, 366, 429
- Yan, M., Sadeghpour, H. R., & Dalgarno, A. 1998, *ApJ*, 496, 1044
- Yoshikawa, K., Itoh, M., & Suto, Y. 1998, *PASJ*, 50, 203
- Yoshikawa, K. & Suto, Y. 1999, *ApJ*, 513, 549

TABLE 3
Chandra DATA

Cluster	R.A. (h m s)	Decl. (d m s)	z	N_{H}^{a} ($\times 10^{20} \text{ cm}^{-2}$)	ObsID	Array	Livetime (ks)
CL0016+1609	00 18 33.5	+16 26 12.5	0.541	4.07	520	I	66
A0068	00 37 06.2	+09 09 33.2	0.255	4.94	3250	I	10
A0267	01 52 42.1	+01 00 35.7	0.230	2.80	1448	I	8
					3580	I	20
A0370	02 39 53.2	-01 34 35.0	0.375	3.06	515	S	66
					7715	I	7
MS0451.6-0305	04 54 11.4	-03 00 52.7	0.550	5.03	529	I	14
					902	S	43
MACSJ0647.7+7015	06 47 50.2	+70 14 54.6	0.584	5.63	3196	I	19
					3584	I	20
A0586	07 32 20.2	+31 37 55.6	0.171	5.15	530	I	10
MACSJ0744.8+3927	07 44 52.8	+39 27 26.7	0.686	5.68	3197	I	20
					3585	I	19
					6111	I	49
A0611	08 00 56.6	+36 03 24.1	0.288	4.99	3194	S	36
A0665	08 30 58.1	+65 50 51.6	0.182	4.24	531	I	9
					3586	I	30
					7700	I	5
A0697	08 42 57.5	+36 21 56.2	0.282	3.41	532	I	8
					4217	I	19
A0773	09 17 52.8	+51 43 38.9	0.217	1.44	533	I	11
					3588	I	9
					5006	I	20
Zwicky 3146	10 23 39.7	+04 11 09.5	0.291	3.01	909	I	46
					9371	I	40
MS1054.5-0321	10 56 59.4	-03 37 34.2	0.826	3.58	512	S	84
MS1137.5+6625	11 40 22.3	+66 08 16.0	0.784	1.21	536	I	117
MACSJ1149.5+2223	11 49 35.5	+22 24 02.3	0.544	2.28	1656	I	18
					3589	I	20
A1413	11 55 18.0	+23 24 17.0	0.142	2.19	537	I	10
					1661	I	10
					5002	I	36
					5003	I	75
					7696	I	5
CLJ1226.9+3332	12 26 57.9	+33 32 47.4	0.890	1.38	932	S	10
					3180	I	32
					5014	I	32
MACSJ1311.0-0310	13 11 01.7	-03 10 38.5	0.490	1.88	3258	I	15
					6110	I	63
					7721	I	7
					9381	I	30
A1689	13 11 29.5	-01 20 28.2	0.183	1.82	540	I	10
					1663	I	11
					5004	I	20
					6930	I	76
					7289	I	75
					7701	I	5
RXJ1347.5-1145	13 47 30.6	-11 45 08.6	0.451	4.85	506	S	9
					507	S	10
					3592	I	57
MS1358.4+6245	13 59 50.6	+62 31 04.1	0.327	1.93	516	S	51
					7714	I	7
A1835	14 01 02.0	+02 52 41.7	0.252	2.32	495	S	19
					496	S	11
					6880	I	117
					6881	I	36
					7370	I	39
MACSJ1423.8+2404	14 23 47.9	+24 04 42.6	0.545	2.83	1657	I	18
					4195	S	115
A1914	14 26 00.8	+37 49 35.7	0.171	0.95	542	I	8
					3593	I	19
A1995	14 52 57.9	+58 02 55.8	0.322	1.42	906	S	57
					7021	I	48
					7713	I	7
A2111	15 39 41.0	+34 25 08.8	0.229	1.93	544	I	10
A2163	16 15 46.2	-06 08 51.3	0.202	12.1/18.7 ^b	545	I	9
					1653	I	71
A2204	16 32 46.9	+05 34 31.9	0.152	5.67	499	S	10
					6104	I	10
					7940	I	77
A2218	16 35 51.9	+66 12 34.5	0.176	3.24	553	I	6
					1454	I	11
					1666	I	44
					7698	I	5

TABLE 3
Chandra DATA

RXJ1716.4+6708	17	16	48.8	+67	12	34.5	0.813	3.70	548	I	52
A2259	17	20	08.5	+27	40	11.0	0.164	3.70	3245	I	10
A2261	17	22	27.1	+32	07	57.8	0.224	3.28	550	I	9
									5007	I	24
MS2053.7-0449	20	56	21.2	-04	37	47.8	0.583	4.96	551	I	44
									1667	I	44
MACSJ2129.4-0741	21	29	26.0	-07	41	28.7	0.570	4.84	3199	I	18
									3595	I	19
RXJ2129.7+0005	21	29	39.9	+00	05	19.8	0.235	4.28	552	I	10
MACSJ2214.9-1359	22	14	57.3	-14	00	12.3	0.483	3.28	3259	I	19
									5011	I	18
MACSJ2228.5+2036	22	28	33.0	+20	37	14.4	0.412	4.58	3285	I	20

^a Dickey & Lockman (1990) values.

^b Both values are considered because A2163 is known to have an N_H significantly different from Dickey & Lockman (1990).

TABLE 4
SPECTROSCOPIC RESULTS

	3.1				4.1				4.2			
	T_e (keV)	Z (Z_\odot)	Λ_{eff}^a	d_A (Gpc)	T_e (keV)	Z (Z_\odot)	Λ_{eff}^a	d_A (Gpc)	T_e (keV)	Z (Z_\odot)	Λ_{eff}^a	d_A (Gpc)
CL0016+1609	9.93 ^{+0.51} _{-0.47}	0.371 ^{+0.081} _{-0.079}	2.502 ^{+0.030} _{-0.028}	1.632 ^{+0.400} _{-0.400}	8.99 ^{+0.39} _{-0.36}	0.345 ^{+0.067} _{-0.065}	2.518 ^{+0.028} _{-0.026}	1.864 ^{+0.451} _{-0.451}	9.39 ^{+0.49} _{-0.41}	0.334 ^{+0.072} _{-0.070}	2.489 ^{+0.028} _{-0.027}	1.740 ^{+0.425} _{-0.425}
A0068	11.28 ^{+1.64} _{-1.19}	0.475 ^{+0.239} _{-0.218}	3.018 ^{+0.099} _{-0.088}	0.509 ^{+0.203} _{-0.203}	8.57 ^{+0.82} _{-0.74}	0.508 ^{+0.176} _{-0.160}	3.066 ^{+0.082} _{-0.075}	0.825 ^{+0.313} _{-0.313}	9.66 ^{+0.99} _{-0.85}	0.597 ^{+0.196} _{-0.174}	3.013 ^{+0.084} _{-0.074}	0.681 ^{+0.259} _{-0.259}
A0267	6.91 ^{+1.32} _{-0.30}	0.530 ^{+0.105} _{-0.104}	2.976 ^{+0.048} _{-0.048}	0.978 ^{+0.303} _{-0.303}	6.24 ^{+0.25} _{-0.27}	0.482 ^{+0.090} _{-0.086}	2.976 ^{+0.037} _{-0.037}	1.122 ^{+0.347} _{-0.347}	6.67 ^{+0.30} _{-0.30}	0.498 ^{+0.095} _{-0.089}	2.934 ^{+0.047} _{-0.044}	1.018 ^{+0.315} _{-0.315}
A0370	8.78 ^{+0.42} _{-0.40}	0.375 ^{+0.079} _{-0.075}	2.263 ^{+0.028} _{-0.026}	1.707 ^{+0.504} _{-0.504}	7.90 ^{+0.37} _{-0.34}	0.403 ^{+0.080} _{-0.079}	2.295 ^{+0.030} _{-0.029}	2.058 ^{+0.608} _{-0.608}	8.14 ^{+0.39} _{-0.38}	0.395 ^{+0.084} _{-0.082}	2.282 ^{+0.030} _{-0.029}	1.955 ^{+0.578} _{-0.578}
MS0451.6-0305	10.78 ^{+0.55} _{-0.53}	0.504 ^{+0.094} _{-0.091}	2.179 ^{+0.029} _{-0.028}	1.641 ^{+0.401} _{-0.401}	9.59 ^{+0.50} _{-0.43}	0.386 ^{+0.076} _{-0.074}	2.175 ^{+0.025} _{-0.024}	1.986 ^{+0.484} _{-0.484}	10.37 ^{+0.54} _{-0.52}	0.426 ^{+0.085} _{-0.081}	2.158 ^{+0.027} _{-0.026}	1.753 ^{+0.430} _{-0.430}
MACSJ0647.7+7015	12.07 ^{+1.22} _{-1.00}	0.367 ^{+0.144} _{-0.138}	2.633 ^{+0.053} _{-0.049}	0.858 ^{+0.271} _{-0.271}	10.06 ^{+0.80} _{-0.69}	0.259 ^{+0.107} _{-0.105}	2.607 ^{+0.045} _{-0.042}	1.130 ^{+0.346} _{-0.346}	11.53 ^{+1.24} _{-0.94}	0.259 ^{+0.130} _{-0.127}	2.550 ^{+0.048} _{-0.044}	0.899 ^{+0.285} _{-0.285}
A0586	7.16 ^{+0.43} _{-0.39}	0.659 ^{+0.141} _{-0.127}	2.956 ^{+0.074} _{-0.060}	0.598 ^{+0.197} _{-0.197}	6.39 ^{+0.34} _{-0.32}	0.582 ^{+0.120} _{-0.110}	2.949 ^{+0.072} _{-0.069}	0.700 ^{+0.229} _{-0.229}	6.67 ^{+0.36} _{-0.35}	0.606 ^{+0.122} _{-0.114}	2.927 ^{+0.068} _{-0.058}	0.658 ^{+0.216} _{-0.216}
MACSJ0744.8+3927	8.99 ^{+0.39} _{-0.39}	0.436 ^{+0.086} _{-0.080}	2.462 ^{+0.033} _{-0.033}	1.667 ^{+0.485} _{-0.485}	8.03 ^{+0.34} _{-0.34}	0.379 ^{+0.068} _{-0.068}	2.441 ^{+0.032} _{-0.032}	1.926 ^{+0.559} _{-0.559}	8.57 ^{+0.37} _{-0.37}	0.411 ^{+0.077} _{-0.075}	2.403 ^{+0.033} _{-0.032}	1.768 ^{+0.513} _{-0.513}
A0611	6.89 ^{+0.27} _{-0.27}	0.393 ^{+0.076} _{-0.073}	2.478 ^{+0.031} _{-0.029}	0.852 ^{+0.254} _{-0.254}	6.28 ^{+0.25} _{-0.24}	0.354 ^{+0.069} _{-0.063}	2.488 ^{+0.031} _{-0.028}	0.990 ^{+0.297} _{-0.297}	6.93 ^{+0.27} _{-0.27}	0.369 ^{+0.075} _{-0.072}	2.449 ^{+0.030} _{-0.029}	0.857 ^{+0.255} _{-0.255}
A0665	8.47 ^{+0.27} _{-0.28}	0.359 ^{+0.061} _{-0.061}	2.983 ^{+0.026} _{-0.026}	0.845 ^{+0.233} _{-0.233}	7.30 ^{+0.18} _{-0.18}	0.319 ^{+0.050} _{-0.050}	2.995 ^{+0.025} _{-0.024}	1.064 ^{+0.292} _{-0.292}	7.96 ^{+0.25} _{-0.25}	0.321 ^{+0.054} _{-0.054}	2.936 ^{+0.025} _{-0.024}	0.923 ^{+0.254} _{-0.254}
A0697	10.50 ^{+0.59} _{-0.57}	0.518 ^{+0.206} _{-0.101}	3.013 ^{+0.044} _{-0.042}	0.872 ^{+0.266} _{-0.266}	9.26 ^{+0.50} _{-0.41}	0.449 ^{+0.088} _{-0.083}	3.042 ^{+0.039} _{-0.036}	1.052 ^{+0.318} _{-0.318}	10.32 ^{+0.56} _{-0.55}	0.481 ^{+0.099} _{-0.095}	2.988 ^{+0.041} _{-0.039}	0.871 ^{+0.265} _{-0.265}
A0773	8.13 ^{+0.32} _{-0.32}	0.509 ^{+0.079} _{-0.076}	3.145 ^{+0.037} _{-0.036}	1.509 ^{+0.438} _{-0.438}	7.25 ^{+0.24} _{-0.21}	0.435 ^{+0.063} _{-0.060}	3.148 ^{+0.033} _{-0.031}	1.772 ^{+0.511} _{-0.511}	7.99 ^{+0.32} _{-0.31}	0.473 ^{+0.067} _{-0.065}	3.095 ^{+0.032} _{-0.031}	1.519 ^{+0.441} _{-0.441}
ZW3146	6.74 ^{+0.10} _{-0.10}	0.477 ^{+0.030} _{-0.029}	2.815 ^{+0.014} _{-0.014}	1.048 ^{+0.329} _{-0.329}	6.00 ^{+0.10} _{-0.09}	0.447 ^{+0.027} _{-0.026}	2.808 ^{+0.014} _{-0.014}	1.227 ^{+0.385} _{-0.385}	6.21 ^{+0.09} _{-0.09}	0.456 ^{+0.028} _{-0.026}	2.784 ^{+0.014} _{-0.014}	1.169 ^{+0.367} _{-0.367}
MS1054.5-0321	11.30 ^{+1.30} _{-0.99}	0.134 ^{+0.132} _{-0.124}	1.862 ^{+0.034} _{-0.027}	1.378 ^{+0.425} _{-0.423}	9.79 ^{+0.84} _{-0.75}	0.142 ^{+0.109} _{-0.105}	1.871 ^{+0.032} _{-0.027}	1.774 ^{+0.522} _{-0.522}	10.39 ^{+0.92} _{-0.83}	0.137 ^{+0.116} _{-0.111}	1.858 ^{+0.033} _{-0.032}	1.618 ^{+0.479} _{-0.479}
MS1137.5+6625	6.54 ^{+0.64} _{-0.55}	0.376 ^{+0.184} _{-0.167}	2.052 ^{+0.062} _{-0.057}	2.586 ^{+0.919} _{-0.919}	6.05 ^{+0.53} _{-0.45}	0.359 ^{+0.168} _{-0.153}	2.035 ^{+0.060} _{-0.056}	2.800 ^{+0.981} _{-0.981}	6.04 ^{+0.56} _{-0.46}	0.352 ^{+0.171} _{-0.151}	2.028 ^{+0.061} _{-0.056}	2.808 ^{+0.989} _{-0.989}
MACSJ1149.5+2223	9.80 ^{+0.77} _{-0.68}	0.244 ^{+0.117} _{-0.110}	2.648 ^{+0.048} _{-0.045}	1.410 ^{+0.423} _{-0.423}	8.92 ^{+0.63} _{-0.55}	0.232 ^{+0.094} _{-0.094}	2.667 ^{+0.045} _{-0.045}	1.600 ^{+0.474} _{-0.474}	9.85 ^{+0.74} _{-0.67}	0.258 ^{+0.103} _{-0.102}	2.625 ^{+0.044} _{-0.042}	1.370 ^{+0.409} _{-0.409}
A1413	7.65 ^{+0.12} _{-0.11}	0.485 ^{+0.028} _{-0.028}	3.295 ^{+0.014} _{-0.014}	0.588 ^{+0.203} _{-0.203}	6.86 ^{+0.08} _{-0.08}	0.450 ^{+0.024} _{-0.023}	3.321 ^{+0.013} _{-0.013}	0.690 ^{+0.238} _{-0.238}	7.46 ^{+0.09} _{-0.09}	0.458 ^{+0.025} _{-0.025}	3.234 ^{+0.007} _{-0.007}	0.605 ^{+0.209} _{-0.209}
CLJ1226.9+3332	14.18 ^{+1.33} _{-1.26}	0.113 ^{+0.139} _{-0.130}	2.337 ^{+0.046} _{-0.033}	1.007 ^{+0.338} _{-0.338}	11.95 ^{+1.14} _{-0.91}	0.169 ^{+0.125} _{-0.123}	2.360 ^{+0.046} _{-0.039}	1.331 ^{+0.442} _{-0.442}	13.10 ^{+1.23} _{-1.06}	0.182 ^{+0.145} _{-0.141}	2.317 ^{+0.050} _{-0.041}	1.152 ^{+0.384} _{-0.384}
MACSJ1311.0-0310	6.50 ^{+0.26} _{-0.24}	0.431 ^{+0.066} _{-0.065}	2.661 ^{+0.032} _{-0.032}	2.115 ^{+0.792} _{-0.792}	5.55 ^{+0.17} _{-0.16}	0.456 ^{+0.064} _{-0.059}	2.627 ^{+0.036} _{-0.033}	2.655 ^{+0.991} _{-0.991}	5.82 ^{+0.19} _{-0.16}	0.466 ^{+0.063} _{-0.061}	2.589 ^{+0.032} _{-0.030}	2.512 ^{+0.938} _{-0.938}
A1689	11.55 ^{+0.12} _{-0.12}	0.324 ^{+0.022} _{-0.021}	3.189 ^{+0.009} _{-0.009}	0.559 ^{+0.141} _{-0.141}	9.76 ^{+0.12} _{-0.11}	0.268 ^{+0.017} _{-0.016}	3.230 ^{+0.008} _{-0.008}	0.736 ^{+0.186} _{-0.186}	10.81 ^{+0.12} _{-0.12}	0.285 ^{+0.018} _{-0.018}	3.152 ^{+0.008} _{-0.008}	0.616 ^{+0.156} _{-0.156}
RXJ1347.5-1145	14.35 ^{+0.39} _{-0.39}	0.553 ^{+0.049} _{-0.048}	2.598 ^{+0.016} _{-0.016}	0.870 ^{+0.267} _{-0.267}	11.81 ^{+0.23} _{-0.23}	0.457 ^{+0.038} _{-0.037}	2.615 ^{+0.014} _{-0.013}	1.205 ^{+0.369} _{-0.369}	13.36 ^{+0.39} _{-0.38}	0.504 ^{+0.044} _{-0.043}	2.566 ^{+0.015} _{-0.015}	0.972 ^{+0.299} _{-0.299}
MS1358.4+6245	7.45 ^{+0.36} _{-0.29}	0.525 ^{+0.085} _{-0.082}	2.433 ^{+0.033} _{-0.032}	1.324 ^{+0.464} _{-0.464}	6.57 ^{+0.25} _{-0.24}	0.501 ^{+0.072} _{-0.070}	2.444 ^{+0.031} _{-0.030}	1.649 ^{+0.575} _{-0.575}	7.08 ^{+0.27} _{-0.26}	0.516 ^{+0.078} _{-0.078}	2.426 ^{+0.032} _{-0.030}	1.469 ^{+0.513} _{-0.513}
A1835	8.54 ^{+0.36} _{-0.36}	0.455 ^{+0.016} _{-0.016}	2.940 ^{+0.007} _{-0.007}	0.695 ^{+0.168} _{-0.168}	7.14 ^{+0.05} _{-0.05}	0.444 ^{+0.014} _{-0.014}	2.948 ^{+0.007} _{-0.007}	0.931 ^{+0.225} _{-0.225}	7.60 ^{+0.07} _{-0.07}	0.451 ^{+0.015} _{-0.015}	2.904 ^{+0.007} _{-0.007}	0.847 ^{+0.205} _{-0.205}
MACSJ1423.8+2404	6.25 ^{+0.15} _{-0.15}	0.578 ^{+0.048} _{-0.045}	2.269 ^{+0.022} _{-0.019}	2.243 ^{+0.841} _{-0.841}	5.77 ^{+0.12} _{-0.11}	0.523 ^{+0.044} _{-0.042}	2.251 ^{+0.021} _{-0.019}	2.521 ^{+0.944} _{-0.944}	6.28 ^{+0.15} _{-0.15}	0.549 ^{+0.046} _{-0.044}	2.235 ^{+0.024} _{-0.024}	2.254 ^{+0.845} _{-0.845}
A1914	11.36 ^{+0.36} _{-0.36}	0.364 ^{+0.065} _{-0.063}	3.116 ^{+0.026} _{-0.026}	0.596 ^{+0.158} _{-0.158}	9.47 ^{+0.29} _{-0.24}	0.372 ^{+0.052} _{-0.051}	3.182 ^{+0.023} _{-0.023}	0.812 ^{+0.214} _{-0.214}	10.50 ^{+0.33} _{-0.34}	0.386 ^{+0.058} _{-0.057}	3.112 ^{+0.024} _{-0.024}	0.678 ^{+0.180} _{-0.180}
A1995	9.09 ^{+0.30} _{-0.30}	0.476 ^{+0.066} _{-0.064}	2.606 ^{+0.025} _{-0.024}	1.034 ^{+0.246} _{-0.246}	7.78 ^{+0.25} _{-0.23}	0.422 ^{+0.051} _{-0.049}	2.610 ^{+0.022} _{-0.021}	1.344 ^{+0.319} _{-0.319}	8.40 ^{+0.27} _{-0.28}	0.434 ^{+0.057} _{-0.054}	2.579 ^{+0.023} _{-0.021}	1.186 ^{+0.282} _{-0.282}
A2111	7.69 ^{+0.94} _{-0.78}	0.364 ^{+0.219} _{-0.194}	2.813 ^{+0.097} _{-0.085}	0.903 ^{+0.440} _{-0.440}	7.31 ^{+0.91} _{-0.73}	0.169 ^{+0.177} _{-0.155}	2.773 ^{+0.079} _{-0.069}	0.921 ^{+0.449} _{-0.449}	7.47 ^{+0.96} _{-0.77}	0.170 ^{+0.181} _{-0.156}	2.750 ^{+0.080} _{-0.059}	0.893 ^{+0.437} _{-0.437}
A2163 ^b	20.98 ^{+0.70} _{-0.69}	0.277 ^{+0.065} _{-0.065}	2.644 ^{+0.022} _{-0.022}	0.247 ^{+0.065} _{-0.065}	14.52 ^{+0.34} _{-0.34}	0.344 ^{+0.041} _{-0.041}	2.782 ^{+0.015} _{-0.015}	0.485 ^{+0.127} _{-0.127}	16.72 ^{+0.48} _{-0.48}	0.353 ^{+0.048} _{-0.048}	2.695 ^{+0.017} _{-0.017}	0.372 ^{+0.097} _{-0.097}
A2163 ^c	12.38 ^{+0.33} _{-0.31}	0.319 ^{+0.037} _{-0.037}	2.545 ^{+0.013} _{-0.012}	0.641 ^{+0.168} _{-0.168}	10.24 ^{+0.19} _{-0.18}	0.318 ^{+0.028} _{-0.027}	2.597 ^{+0.010} _{-0.010}	0.884 ^{+0.230} _{-0.230}	11.21 ^{+0.19} _{-0.19}	0.334 ^{+0.031} _{-0.030}	2.543 ^{+0.011} _{-0.011}	0.755 ^{+0.196} _{-0.196}
A2204	8.06 ^{+0.09} _{-0.09}	0.578 ^{+0.022} _{-0.021}	3.034 ^{+0.010} _{-0.010}	1.224 ^{+0.333} _{-0.333}	6.49 ^{+0.06} _{-0.05}	0.556 ^{+0.019} _{-0.018}	3.042 ^{+0.009} _{-0.009}	1.761 ^{+0.479} _{-0.479}	6.92 ^{+0.06} _{-0.06}	0.562 ^{+0.020} _{-0.020}	2.986 ^{+0.009} _{-0.009}	1.592 ^{+0.433} _{-0.433}
A2218	7.23 ^{+0.13} _{-0.18}	0.269 ^{+0.056} _{-0.054}	2.875 ^{+0.026} _{-0.024}	1.524 ^{+0.405} _{-0.405}	6.55 ^{+0.17} _{-0.17}	0.263 ^{+0.046} _{-0.046}	2.898 ^{+0.024} _{-0.024}	1.747 ^{+0.466} _{-0.466}	6.92 ^{+0.17} _{-0.17}	0.246 ^{+0.051} _{-0.049}	2.855 ^{+0.024} _{-0.024}	1.596 ^{+0.426} _{-0.426}
RXJ1716.4+6708	6.29 ^{+0.78} _{-0.66}	0.867 ^{+0.319} _{-0.263}	2.215 ^{+0.127} _{-0.108}	2.222 ^{+1.134} _{-1.134}	5.96 ^{+0.62} _{-0.62}	0.748 ^{+0.278} _{-0.229}	2.175 ^{+0.103} _{-0.103}	2.276 ^{+1.163} _{-1.163}	6.10 ^{+0.66} _{-0.66}	0.773 ^{+0.273} _{-0.239}	2.176 ^{+0.119} _{-0.105}	2.214 ^{+1.135} _{-1.135}
A2259	5.35 ^{+0.28} _{-0.27}	0.400 ^{+0.129} _{-0.116}	2.992 ^{+0.084} _{-0.069}	0.629 ^{+0.457} _{-0.457}	4.88 ^{+0.26} _{-0.24}	0.325 ^{+0.113} _{-0.}						